



JGR Planets

RESEARCH ARTICLE

10.1029/2020JE006715

Key Points:

- No evidence for lunar fields >7 μ T at \approx 3.1 Ga
- Initial lunar dynamo decline spanning ≈370 Ma indicates two stability regimes
- Grain size may control magnetic fidelity in lunar rocks

Supporting Information:

Supporting Information may be found in the online version of this article.

Correspondence to:

B. E. Strauss, beck.strauss@nist.gov

Citation:

Strauss, B. E., Tikoo, S. M., Gross, J., Setera, J. B., & Turrin, B. (2021). Constraining the decline of the lunar dynamo field at ≈3.1 Ga through paleomagnetic analyses of Apollo 12 mare basalts. *Journal of Geophysical Research: Planets*, 126, e2020JE006715. https://doi.org/10.1029/2020JE006715

Received 30 SEP 2020 Accepted 5 JAN 2021 Corrected 22 JULY 2021

The copyright line for this article was changed on 22 JULY 2021 after original online publication.

Author Contributions:

Conceptualization: B. E. Strauss, S. M. Tikoo

Data curation: B. E. Strauss, J. B. Setera **Formal analysis:** B. E. Strauss, S. M.

Tikoo, J. Gross, J. B. Setera, B. Turrin Funding acquisition: S. M. Tikoo Investigation: B. E. Strauss, S. M. Tikoo, J. Gross, J. B. Setera, B. Turrin Methodology: B. E. Strauss, S. M. Tikoo, J. Gross, J. B. Setera, B. Turrin Project Administration: S. M. Tikoo Resources: S. M. Tikoo, J. Gross, B.

Supervision: S. M. Tikoo, J. Gross

© 2021. American Geophysical Union. All Rights Reserved. This article has been contributed to by US Government employees and their work is in the public domain in the USA.

Constraining the Decline of the Lunar Dynamo Field at ≈3.1 Ga Through Paleomagnetic Analyses of Apollo 12 Mare Basalts

B. E. Strauss^{1,2}, S. M. Tikoo^{1,3}, J. Gross^{1,4,5}, J. B. Setera^{1,6}, and B. Turrin¹

¹Department of Earth and Planetary Science, Rutgers University, Piscataway, NJ, USA, ²Materials Science and Engineering Division, National Institute of Standards and Technology, Gaithersburg, MD, USA, ³Department of Geophysics, Stanford University, Stanford, CA, USA, ⁴Department of Earth and Planetary Sciences, The American Museum of Natural History, New York, NY, USA, ⁵Lunar and Planetary Institute, Houston, TX, USA, ⁶Department of Earth and Atmospheric Sciences, Cornell University, Ithaca, NY, USA

Abstract Recent paleomagnetic studies of lunar rocks have suggested that the magnetic field of the Moon reached peak intensities on the order of \approx 77 μ T between 3.85 billion and 3.56 billion years ago (Ga) and subsequently declined to surface intensities of \approx 4 μ T by 3.19 Ga. However, this decline in the intensity of the lunar field has only been shown in a small number of samples, presenting challenges for constraint of its timing and thus the dynamo generation mechanisms that could be responsible. We present microscopic and magnetic analyses of Apollo samples 12008, 12009, and 12015, three fine-grained mare vitrophyre basalts with high magnetic fidelity, indicating that these samples were not magnetized in conditions consistent with a planetary magnetic field exceeding 4–7 μ T during their formation. We further report updated radiometric ages for samples 12008 and 12009 and the first-ever radiometric age for sample 12015, dating this lunar field intensity constraint to \approx 3.1 Ga. These data are consistent with results of previous work on the initial decline of the Moon's magnetic field and confirm that the mechanism of lunar dynamo generation changed dramatically between 3.6 and 3.1 Ga.

Plain Language Summary Although the Moon does not have a magnetic field in the present day, records of an ancient lunar field have been found in rock samples collected during the Apollo missions. Between 3.85 billion and 3.56 billion years ago, the Moon's magnetic field was as strong as the Earth's field is today, but samples from 3.19 billion years ago have shown records of a much weaker field. To understand what caused this change in the strength of the field, we need evidence from more samples capable of recording weak magnetic fields around when the field declined. In this study, we analyzed three volcanic rock samples from the Moon and showed that all three are able to record weak magnetic fields, but none of them recorded such fields when they formed. We also determined the ages of these rocks and found that they are all about 3.1 billion years old. This means that 3.1 billion years ago, the Moon had an extremely weak magnetic field. This conclusion agrees with previous studies and confirms that the strength of the field changed very quickly, which must have been the result of a rapid and major change in how the field was produced.

1. Introduction

The strength and longevity of the Moon's dynamo field have been topics of debate since its existence was first suggested more than 40 years ago. Initial paleomagnetic studies of lunar samples from the Apollo missions indicated that the Moon may have generated a core dynamo that persisted to at least 3.7 billion years ago (Ga) (Cisowski & Fuller, 1986), though it was later suggested that the dynamo may have lasted until at least 3.2 Ga (Runcorn, 1996). Recent paleomagnetic studies indicate that a lunar dynamo indeed existed between at least 4.25 and 1.92 Ga (Cournède et al., 2012; Garrick-Bethell et al., 2009, 2017; Mighani et al., 2020; Shea et al., 2012; Suavet et al., 2013; Tikoo et al., 2017) and that a high field period (mean surface field intensity \approx 77 μ T, 2σ uncertainty factor \approx 2.2) occurred between 3.85 and 3.56 Ga (Weiss & Tikoo, 2014), followed by an apparent decline in surface intensity to below \approx 4 μ T by 3.19 Ga (Tikoo et al., 2014).

Subsequent work by Tikoo et al. (2017) and Mighani et al. (2020) suggests that this order-of-magnitude decline in lunar paleointensities between 3.56 and 3.19 Ga was the first of two declines, marking the beginning

STRAUSS ET AL. 1 of 21



Validation: B. E. Strauss, S. M. Tikoo, J. Gross, J. B. Setera
Visualization: B. E. Strauss, B. Turrin
Writing – original draft: B. E. Strauss
Writing – review & editing: B. E.
Strauss, S. M. Tikoo, J. Gross, J. B. Setera

of a low field period (surface field intensities $\approx 5 \,\mu T$) that lasted until the second and final period of decline $\approx 1-2$ Ga that marked the cessation of the lunar dynamo. A change in state from the high field period to the low field period suggests that a change in the mechanism of lunar field generation may have occurred between 3.56 Ga and ≈ 3.2 Ga, with two explanations offered: either (1) two distinct dynamo generation mechanisms were in operation, with the first generating a strong field until its collapse and the second sustaining a weak field until $\approx 1-2$ Ga, or (2) a single dynamo mechanism was bistable, transitioning from a high field state to a low field state (Mighani et al., 2020; Tikoo et al., 2017; Weiss & Tikoo, 2014).

Although the particular mechanism(s) of lunar field generation have not yet been conclusively identified, thermal evolution models have suggested several mechanisms with varying duration and intensity. While thermal convection could generate a magnetic field until \approx 3.5 Ga (Evans et al., 2014; Konrad & Spohn, 1997; Stegman et al., 2003), thermochemical convection produced by core crystallization could account for a longer-lived field lasting until \approx 1 Ga (Laneuville et al., 2014; Mighani et al., 2020; Scheinberg et al., 2015; Zhang et al., 2013). However, thermal and thermochemical core dynamos are both incapable of continuously sustaining the >10 μ T fields inferred for the high field period (Evans et al., 2018), suggesting that alternative dynamo generation mechanisms may be required. Impact-driven stirring of the core may produce transient dynamos, lasting for only a few thousand years after individual basin-forming impacts (Le Bars et al., 2011), but it is unlikely to explain any lunar magnetism after \approx 3.7 Ga (Suavet et al., 2013).

Mantle precession could have generated a mechanical dynamo producing ≈ 10 –100 μT fields from the Cassini transition until the Moon reached a semimajor axis of ≈ 42.5 Earth radii (R_e), although this timing depends on the largely unconstrained evolution of the lunar orbit; models have constrained this window to ≈ 3 –4 Ga (Dwyer et al., 2011; Stanley et al., 2017). Viscous friction produced by precession of the inner core may bolster a thermally convective dynamo, enabling a weak ≈ 5 μT surface field to persist beyond the lifetime of a dynamo generated by mantle precession until ≈ 1 Ga. However, precession at the inner core boundary alone cannot explain the high field epoch, as the maximum field strength produced solely by this mechanism early in lunar history is only ≈ 10 μT and decreases over time (Stys & Dumberry, 2020). A basal magma ocean has been proposed to account for strong surface fields during the same time period (Scheinberg et al., 2018) but the expected low conductivity of the silicate minerals that dominate the lunar interior makes the feasibility of this mechanism uncertain.

An improved understanding of the timing and rate of decline of the lunar dynamo field will help to constrain this list of candidate mechanisms, according to the longevity and intensity potential of each mechanism. However, the poor magnetic recording properties of most lunar igneous rocks have hindered prior attempts to retrieve paleomagnetic records from samples <3.56 Ga, which were likely magnetized in relatively weak fields (Tikoo et al., 2012). Apollo-era paleomagnetic studies were plagued by the conflation of poor paleomagnetic recorders with well-recorded weak paleofields, while recent studies (Table 1) use more rigorous paleointensity methods that more effectively differentiate between these phenomena. However, the timing of the initiation of the low field epoch is still poorly constrained by modern experimental studies, with no reliable data available during the period between 3.56 and 3.4 Ga and few data points after. Furthermore, during the high field epoch, order-of-magnitude scatter in paleointensities has been observed in rocks that are approximately the same age (Weiss & Tikoo, 2014); this suggests that the analysis of additional younger samples could reveal scatter that has not previously been observed in <3.56 Ga rocks.

To better characterize the process of lunar field decline, more analyses must be conducted on samples aged <3.56 Ga that have sufficiently high magnetic fidelity to constrain the weakening lunar field during its transition from high to low intensity conditions. The difficulty of retrieving reliable paleointensities from mare basalts initially magnetized in paleofields $<50~\mu T$ has previously been attributed to a combination of multidomain (MD) ferromagnetic grain sizes and the effects of magnetic anisotropy (Tikoo et al., 2012, 2014). Because vitrophyric basalts initially cooled below their Curie temperatures at faster rates (hours to days) than more crystalline mare basalts (days to weeks), vitrophyres may contain smaller, higher-fidelity magnetic grains (i.e., single domain [SD] sized grains) and could therefore be capable of acquiring and retaining records of weaker lunar fields, such as those expected to be present during the initial period of field decline and the subsequent low field epoch.

STRAUSS ET AL. 2 of 21



Table 1Previously Published Constraints on the Lunar Paleofield by Age, as Plotted in Figure 6

Sample	Age (Ga)	Paleointensity (μT)	Uncertainty range (μT)	Method	References
76535	4.25	40	20-80	sIRM	Garrick-Bethell et al. (2009); Garrick-Bethell et al. (2017)
71505	≈3.85	95	47.5–190	sIRM	Stöffler et al. (2006); Cournède et al. (2012)
71567	≈3.75	111	55.5–222	sIRM	Stöffler et al. (2006); Cournède et al. (2012)
10020	3.72	66	±37 (reported)	sIRM	Shea et al. (2012)
70017	3.67	42	21-84	sIRM	Cournède et al. (2012)
10017	3.59	71	35.5–142	sIRM	Suavet et al. (2013)
10049	3.56	77	38.5–154	sIRM	Suavet et al. (2013)
60015	3.46	<5	-	Thellier-IZZI	Lawrence et al. (2008); Tikoo et al. (2014) [Shocked (Tikoo et al., 2014)]
15475	3.4	N/A	-	sIRM	Cournède et al. (2012) [Remagnetized]
12017 basalt	3.36	<37	≤74	ARM	Tikoo et al. (2012); Tikoo et al. (2014); Buz et al. (2015)
12002	3.3	≈50	-	sIRM	Cournède et al. (2012) [Experimental issues (Suavet et al., 2013; Tikoo et al., 2014)]
15597	≈3.3	<7	≤14	ARM	Tikoo et al. (2014)
15016	3.281	<37	≤74	ARM	Tikoo et al. (2012); Tikoo et al. (2014); Shuster and Cassata (2015)
15556	3.233	<75	≤150	ARM	Tikoo et al. (2012); Tikoo et al. (2014); Shuster and Cassata (2015)
12022	3.194	<4	≤8	ARM	Tikoo et al. (2014)
12015	3.165	<4	-	ARM	This study
12009	3.159	< 7	-	ARM	This study
12008	3.061	<7	-	ARM	This study
15498	≈1.92-1.02	5	±2 (reported)	Thellier-IZZI	Tikoo et al. (2017); Mighani et al. (2020)
15015	0.91	<0.08, <0.7	≤0.16	ARM, Thellier-IZZI	Mighani et al. (2020)
15465	0.44	<0.06, <0.4	≤0.12	ARM, Thellier-IZZI	Mighani et al. (2020)
12017 glass	<0.007	<7	≤14	ARM	Tikoo et al. (2012); Tikoo et al. (2014); Buz et al. (2015)

Notes. In the Paleointensity column, numbers with < indicate paleointensity fidelity limits (μ T). In the Uncertainty Range column, multiplicative factor 2 uncertainties are calculated from provided paleointensity averages in each source study unless otherwise indicated. In the Method column, ARM, anhysteretic remanent magnetization; sIRM, saturation isothermal remanent magnetization; Thellier-IZZI, following the alternating in-field, zero-field, zero-field, in-field (IZZI) protocol methods of Tauxe and Staudigel (2004). Italicized samples are not used in this study and are included in this table for completeness.

In this study, we investigate whether records of weak magnetic fields can be retrieved from lunar vitrophyres <3.56 Ga. We then assess whether these records indicate a real decline in the lunar paleofield or can be explained by small number statistics due to the relatively low number of Apollo samples analyzed to date using modern paleomagnetic techniques.

STRAUSS ET AL. 3 of 21



2. Methods

2.1. Samples

Mare basalt samples 12008, 12009, and 12015 were collected in the southeastern region of Oceanus Procellarum during the Apollo 12 mission (see Rhodes et al., 1977). All three samples are fine-grained olivine vitrophyres (Meyer, 2011). Thin sections 12008,41, 12009,11, and 12015,43, and parent chips 12008,72 (1.852 g), 12009,156 (2.469 g), and 12015,40 (2.917 g) were obtained from Johnson Space Center (JSC) in 2012. 12008, 12009, and 12015 have not previously been cut via circular saw, precluding any saw cutting-induced thermal overprints (e.g., Mighani et al., 2020; Tikoo et al., 2014). The rocks were stored in the magnetically shielded room at the MIT Paleomagnetism Laboratory for five years prior to our initial analyses and were transferred to the magnetically shielded room at the Rutgers Paleomagnetism Laboratory in 2017.

2.2. Electron Probe Microanalyses

Initial petrographic investigations of thin sections 12008,41, 12009,11, and 12015,43 were conducted via a petrographic microscope. Additional thin section images were obtained from the Virtual Microscope, a publicly accessible compendium of thin sections from Apollo samples (Open University, 2018). In addition to these thin sections, we also prepared and studied one thick section from each sample. One slice (see Section 2.4) of each parent chip was subdivided, mounted as a thick section in methyl methalacrylate resin (Dentsply Sirona [Certain commercial equipment, instruments, materials, and software are identified in this paper to foster understanding. Such identification does not imply recommendation or endorsement by the National Institute of Standards and Technology, nor does it imply that the materials or equipment identified are necessarily the best available for the purpose]), and polished on both sides for microprobe analyses.

Quantitative electron probe microanalyses (EPMA) were performed on all three thin sections and all three thick sections using the JEOL JXA-2800 Superprobe at Rutgers University in the Department of Earth and Planetary Sciences. Metal analyses were conducted using an acceleration voltage of 15 kV, a beam current of 25 nA, and a focused (<1 μm) beam diameter. Matrix analyses were conducted using an acceleration voltage of 15 kV, a beam current of 25 nA, and a defocused 10 μm beam diameter. Peak counting times for both setups were 10 s for Na and K; 30 s for Ca, Si, Mg, Al, Mn, Fe, and Ni; 60 s for Co, S, and P. Probe for EPMA software mean atomic number (MAN) protocol was used for background measurements (Donovan et al., 2016) and the standard ZAF (atomic number, absorption, and characteristic fluorescence) correction was applied to the data. Secondary standards were analyzed at regular intervals throughout each session to correct for potential drift. Analytical standards were well-characterized natural and synthetic oxides and minerals including orthoclase (K), forsterite (Mg), Co-foil (Co), jadeite (Na), quartz (Si), spinel (Al), anorthite (Ca), tephroite (Mn), troilite (S, Fe), apatite (P), Ni-olivine (Ni), chromite (Cr), and rutile (Ti). Data quality was ensured by analyzing secondary standards as unknowns.

Detection limits at 3σ (99% confidence level) and analytical errors (%) were obtained from the Probe for EPMA program (Donovan et al., 2016). For metal analyses, average detection limits (in elemental mass %) are: K=0.02; Na=0.03; Si, Mg, Si, S

Backscattered electron (BSE) images and qualitative elemental X-ray maps were taken using the JEOL JXA-8200 Superprobe at Rutgers University. For metal grains, an accelerating voltage of 15 kV, beam current of 25 nA, dwell time of 50 ms, focused (<1 μ m) beam diameter, and step size ranging from 0.5 to 1 μ m were used. Wavelength dispersive spectrometers (WDS) were used to map for (K α) Ti, Si, Ni, Co, and S. Cr, P, Fe, Mg, and Al were mapped simultaneously using the energy dispersive X-ray spectrometer (EDS). For qualitative elemental X-ray maps of the matrix, an accelerating voltage of 15 kV, beam current of 30 nA, dwell

STRAUSS ET AL. 4 of 21



time of 50 ms, focused (<1 μ m) beam diameter, and pixel step size between 3 and 5 μ m were used. WDS was used to map for (K α) Na, Al, Fe, K, and Si; EDS was used to map for Ca, Mg, Ni, and S. All elemental analyses were performed on larger (\gtrsim 10 μ m) grains to avoid overlapping analyses.

2.3. Dating

Previous attempts to obtain 40 Ar/ 39 Ar ages for 12008 and 12009 have been complicated by anomalous age spectra wherein low temperature release steps have higher apparent ages than higher temperature release steps (McDougall & Harrison, 1977; Stettler et al., 1973). These age spectra are similar to that of the impact melt glass rind of Apollo 12 mare basalt 12017 (Buz et al., 2015) and polymict breccia 12013 (Turner, 1971). Stettler et al. (1973) attribute this phenomenon to the high glass content of samples 12008 and 12009, while Turner (1971) points to devitrification, which could produce sites with low apparent ages due to localized argon loss. Nevertheless, Stettler et al. (1973) report 40 Ar/ 39 Ar total fusion ages for samples 12008 (3180 \pm 70 Ma and 3090 \pm 70 Ma) and 12009 (3290 \pm 70 Ma and 3170 \pm 70 Ma), although the release spectra did not yield a plateau age for either sample. These reported total fusion ages for 12008 and 12009 are close to the 3.22 \pm 0.04 Ga 40 Ar/ 39 Ar plateau ages of the rest of the Apollo 12 olivine mare basalt group (Stöffler et al., 2006) and were therefore expected to be similar to their true crystallization ages. No 40 Ar/ 39 Ar results have previously been published for sample 12015 (Meyer, 2011). The acquisition of precise and accurate ages for all three samples is crucial for the contextualization of their magnetic remanence in the existing timeline of lunar paleointensities, particularly with respect to the initial period of lunar field decline.

We used the elemental maps produced through the microprobe analyses described above as a guide to micro-mill out K-rich zones from each thick section. The resulting fragments were used as 40 Ar/ 39 Ar radiometric dating aliquots to obtain the crystallization ages of all three Apollo 12 basalts. 40 Ar/ 39 Ar step heating has been applied successfully to glassy material from other lunar samples (e.g., the matrix of 12022 [Tikoo et al., 2014] and the glass spatter portion of 12017 [Buz et al., 2015]), although these studies relied on either whole rock aliquots or small numbers of aliquots. In contrast, the micro-milling technique used to collect fragments from rock slices that had already been used for EPMA allows for the analysis of a larger number of aliquots from known source locations in a sample, using elemental maps to more precisely describe the material included in each aliquot. We studied three aliquots from 12008, five aliquots from 12009, and 12 aliquots from 12015.

The step-heating method and the evaluation of the release spectra facilitate the examination of the 40 K (via the 39 Ar_(K) proxy) and radiogenic 40 Ar distribution within the sample over the temperature range from ≈ 500 °C to fusion (Turrin et al., 2008). In addition, the distribution of the apparent ages of the release spectra can be evaluated relative to the atomic K/Ca ratios determined from the K and Ca proxies 39 Ar_K and 37 Ar_{Ca} respectively. 40 Ar/ 39 Ar total fusion ages (integrated ages) do not yield this type of information, and thus can lead to difficulties interpreting the data.

The ⁴⁰Ar/³⁹Ar noble gas measurements were obtained at Rutgers University using a custom built micro-noble gas extraction system (see Carr et al., 2007 for description) in line with an upgraded Mass Analyzer Product (MAP) 215-50 noble gas mass spectrometer with a digital ion-counting secondary electron multiplies (Turrin et al., 2010). All samples were loaded into pits drilled into 1 cm diameter Al disks for neutron irradiation, together with the reference mineral standards Fish Canyon sanidine (FC-2) (Kuiper et al., 2008), Hb3gr hornblende (Jourdan & Renne, 2007; Machlus et al., 2020), and an internal blind laboratory sanidine standard (≈315 million year old (Ma) sanidine from the Carboniferous Fire Clay tonstein, a U-Pb dated tuff) (Lyons et al., 2006). The pits are arranged in a controlled geometry to facilitate the correction of any measurable gradients in the neutron flux. Neutron irradiation was carried out at the Cd-shielded CLICIT facility of the Oregon State University TRIGA reactor for 80 h, with fluence monitor standards producing a nominal J-value ranging from 2.11910×10^{-2} to 2.12506×10^{-2} for the samples in this study. After irradiation, samples were heated incrementally using a 40 watt New Wave CO2 laser system. A coaxial video camera with low resolution and a slightly off-axis two-color IR optical pyrometer were used to digitally image and record the step-heating process and the temperatures respectively (e.g., Setera et al., 2020). A typical ten-minute static system "cold" blank (10^{-18} mol) is: 40 Ar = 714 ± 30, 39 Ar = 13.3 ± 1.0, 38 Ar = 1.1 ± 0.5, 37 Ar = 24 ± 0.2, 36 Ar = 3.6 \pm 0.1. Instrumental mass fractionation was monitored by analyzing a known volume of atmospheric Ar after every eighth sample and blank measurement. Data reduction was implemented using

STRAUSS ET AL. 5 of 21



automated software written by A. Deino of the Berkeley Geochronology Center. Initial age calculations incorporate the decay constants of Steiger and Jäger (1977). However, for consistency with the majority of published lunar geochronology, all ages within the main text are recalculated with the decay constants of Renne et al. (2011) using the equations of Mercer and Hodges (2016).

We define a 40 Ar/ 39 Ar plateau age as the inverse variance-weighted mean of three or more consecutive steps with apparent ages that agree within the 95% confidence interval and which, taken together, represent \geq 50% of the 39 Ar released (Dalrymple & Lanphere, 1969, 1974; Fleck et al., 1977; Taylor, 1997). Uncertainties are expressed at the 1σ level unless otherwise specified.

2.4. Rock Magnetism and Paleomagnetism

Apollo samples 12008 and 12015 have not previously been characterized through magnetic techniques (see summary in Meyer (2011)). A chip from sample 12009 was subjected to paleomagnetic analysis and characterization by Fuller et al. (1979), who found that this sample contained a mixture of soft and hard magnetic phases, but concluded that its remanent magnetization was dominated by a large low-coercivity component "so unstable" that NRM interpretation would not be useful.

Paleomagnetic studies were conducted on pristine material from each sample. Sample preparation for magnetic analyses was conducted at the Massachusetts Institute of Technology (MIT) Paleomagnetism Laboratory and the Rutgers Paleomagnetism Laboratory. Each parent chip was cut into six mutually oriented $\approx 0.1-0.2$ g subsamples using a Well 3500 precision diamond wire saw lubricated with isopropyl alcohol to reduce the likelihood of spurious remagnetization through heating or chemical alteration. Five slices from each sample were individually mounted with cyanoacrylate cement (Loctite) on quartz discs, while the sixth slice was reserved for microscopic and chemical analyses.

All magnetic characterization was conducted at room temperature. Hysteresis loops and backfield remanence curves were collected using the Princeton Measurements Corporation MicroMag 2900 AGM Magnetometer at Rutgers University. Three to four small (\approx 0.02 g) chips of each sample were subjected to a series of three to five hysteresis loops and one to two backfield curves. Diamagnetic and paramagnetic contributions were corrected using the IRMDB software provided by the Institute for Rock Magnetism, University of Minnesota.

Paleomagnetic analyses were conducted on two 2G Superconducting Rock Magnetometer 755 RAPID systems with sensitivities of 10^{-12} Am², housed at the MIT Paleomagnetism Laboratory and the Rutgers University Paleomagnetism Laboratory. To analyze the natural remanent magnetization (NRM) and determine whether our rocks hold a record of ancient lunar fields, five subsamples from each parent sample were subjected to identical stepwise three-axis alternating field (AF) demagnetization and measurement up to maximum fields of 110 mT (Rutgers) or 145 mT (MIT), or until moments were reduced beyond the noise level of the magnetometer.

All paleomagnetic experiments were conducted at room temperature to circumvent thermal alteration, which must be carefully avoided in studies of irreplaceable lunar material. However, AF methods can introduce unwanted secondary magnetizations in the form of anhysteretic remanent magnetization (ARM) and gyroremanent magnetization (GRM) (Garrick-Bethell et al., 2009; Tikoo et al., 2012). These spurious signals increase in intensity with increasing peak fields (higher demagnetization steps), ultimately overwhelming the sample's NRM and effectively limiting the recoverable paleointensity (Tikoo et al., 2014). To reduce the effects of acquisition of spurious GRM and ARM, demagnetization data were processed following the Zijderveld-Dunlop protocol: magnetic moments measured after AF application in each of three orthogonal directions were averaged to produced a final moment for each AF level (Garrick-Bethell et al., 2009; Stephenson, 1993; Tikoo et al., 2012). Paleomagnetic data were processed using the PaleoMag 3.1 software package.

2.4.1. Viscous Remanence

Tikoo et al. (2014) noted that in sample 12022, low-coercivity and/or low-temperature components were grouped within each parent block, but were scattered between multiple parent blocks, indicating their likely origin as a viscous remanent magnetization (VRM) acquired in the Earth's magnetic field after cutting at JSC in the 1970s. A VRM acquired over ≈50 years of storage in a non-zero-field environment should be

STRAUSS ET AL. 6 of 21



approximately unidirectional when compared between samples that were stored in the same orientation relative to the ambient field (i.e., from the same parent chip that was only recently cut apart into oriented subsamples) and non-unidirectional across those that were stored in different orientations (i.e., multiple parent chips cut from the same rock upon arrival at JSC). However, Tikoo et al. (2017) described non-unidirectional low- and mid-coercivity components in subsamples from sample 15498 and attributed these disparate orientations and intensities of VRM to both compositional heterogeneity, which could give rise to differing rates of VRM acquisition in the glassy and lithic portions of the parent rock, and physical rotation of the parent chip (and, later, its constituent subsamples) during sampling and storage.

To assess the possibility of a terrestrial VRM origin for magnetization, we conducted a series of laboratory VRM acquisition experiments on subsamples 12008,72d,12009,156h, and 12015,40h following the methods of Tikoo et al. (2017). These three samples were placed in the Earth's field outside of the shielded room in the Rutgers Paleomagnetism Laboratory in a fixed position for ≈ 1 week (5 d 22 h 38 min for 12008,72d; 6 d 22 h 38 min for 12009,156h; 7 d 22 h 38 min for 12015,40h). Each subsample was then returned to the shielded room and, after an 18-34 s delay, measured to determine the intensity of the acquired VRM. Subsample magnetizations were repeatedly measured over the following five days to assess the decay of this VRM with time.

2.5. Paleointensity

In early lunar paleointensity studies, it was often unclear whether poor NRM behavior was due to formation in a weak field or to poor magnetic recording properties, and whether stable NRM behavior could be attributed to formation in a strong field or acquisition of spurious secondary remanence (Tikoo et al., 2012). The conflation of these features led to the inference of anomalously high paleofield strengths, especially in the last 1.5 Ga (Buz et al., 2015; Tikoo et al., 2012, 2014). We therefore experimentally determined each of our samples' paleointensity fidelity threshold, the minimum magnetizing field intensity required for accurate field retrieval using AF methods, to assess the reliability of our samples as magnetic recorders.

One subsample of each parent chip was imparted with a laboratory ARM as a room temperature analogue for TRM, and the resulting remanence was AF demagnetized following the same sequence used for demagnetization of NRM. In an ideal paleomagnetic recorder, the relationship between induced field strength and retrieved paleointensity values is one-to-one. Deviations from this relationship indicate the imperfection of a given recorder.

Laboratory ARMs were produced using an AC peak field of 250 mT and DC fields ranging from 5 to 50 μ T, corresponding to TRM-equivalent fields ranging from 3.7 to 37.3 μ T (using the TRM/ARM ratio of 1.34, below). Following Tikoo et al. (2012); Tikoo et al. (2014), we used the ARM method to retrieve "paleointensities" (P_{ARM}) from each laboratory-induced magnetization:

$$P_{\text{ARM}} = \frac{\Delta \text{NRM}}{\Delta \text{ARM}} \cdot \frac{b}{f'} \tag{1}$$

where Δ NRM and Δ ARM are the changes in moment between AF demagnetization steps for NRM and ARM respectively, b is a DC bias field, and f' is the TRM/ARM ratio. Experimentally determined values of f' for multidomain kamacite are log-normally distributed and range between 0.94 and 1.79 (at 2σ uncertainty), with a mean value of 1.31 (Weiss & Tikoo, 2014). Here we use a value of 1.34 for f', based on the experimental determinations of Stephenson and Collinson (1974). While f' values have not been directly determined for martensite-dominated samples, we do not expect significant differences from kamacite f' values for two reasons: First, kamacite and martensite have similar rock magnetic properties (Kletetschka & Wieczorek, 2017). Second, Stephenson and Collinson (1974) determined that for a single lunar breccia sample (which is likely dominated by martensite given its impact lithology), an obtained Thellier-Thellier paleointensity value and an ARM paleointensity value (obtained using f' = 1.34) differed by only 17%. We calculate paleointensities only using AF levels above which any secondary or low-coercivity components were present in each sample (Tikoo et al., 2014).

STRAUSS ET AL. 7 of 21



Table 2Average Composition of Mesostasis in 12008,72, 12009,11, and 12015,40 Measured by Electron Microprobe; n=10 for Each Sample (Full Results in Table S2)

Oxide (mass %)	12008,72	12009,11	12015,40	
SO ₃	0.22	0.25	0.22	
P_2O_5	0.10	0.10	0.08	
SiO_2	45.92	46.73	47.99	
TiO ₂	6.21	3.48	3.62	
Al_2O_3	10.81	10.43	10.90	
Cr_2O_3	0.51	0.55	0.52	
CaO	16.26	15.25	14.97	
MgO	4.72	5.28	5.36	
FeO	14.73	16.70	16.21	
MnO	0.23	0.28	0.26	
NiO	0.00	0.00	0.00	
CoO	0.00	0.00	0.00	
K_2O	0.03	0.06	0.08	
Na ₂ O	0.19	0.23	0.23	
Total	99.93	99.35	100.46	

3. Results

3.1. Petrography and Electron Probe Microanalyses

All three samples host large (up to 0.5 mm) sub-to euhedral olivine phenocrysts in an opaque glassy matrix (Table 2), with accompanying skeletal or elongate pyroxene phenocrysts (Figure 1). Opaque phenocrysts include angular chromite (<50 μm) and small ($\lesssim\!20~\mu m$ in diameter) bright round grains of another metallic phase, suggested by previous studies to be iron (Brett et al., 1971; Dungan & Brown, 1977; Meyer, 2011). Although troilite has been found in other magnetized lunar basalts (e.g., Dunn et al., 1981; Haggerty et al., 1970), Brett et al. (1971) found no troilite in samples 12008 and 12009. We observed micrometer-scale grains containing Fe and S that may represent troilite (e.g., Figures 2d and 2h), but these grains were too small for conclusive identification through WDS analysis.

Sixty-two of the round grains were mapped with EPMA (11 grains from 12008, 31 grains from 12009, and 20 grains from 12015; representative examples shown in Figure 2) and quantitative points were obtained from 28 of those grains (Table 3). These metal grains have a range of Fe-Ni compositions consistent with kamacite, defined by Ni % by mass fraction <5 (1 grain), and martensite, defined by compositions with $5 \le Ni$ mass % < 25 (Tikoo et al., 2014, 2017; Uehara et al., 2011) (26 grains). Of the 62 grains analyzed, 36 have homogeneous compositions, while 22 show gradients of Ni distribution (Figures 2c, 2g, and 2k). Also visible in BSE imagery of mesostasis glass (Figure 1d) and elemental maps

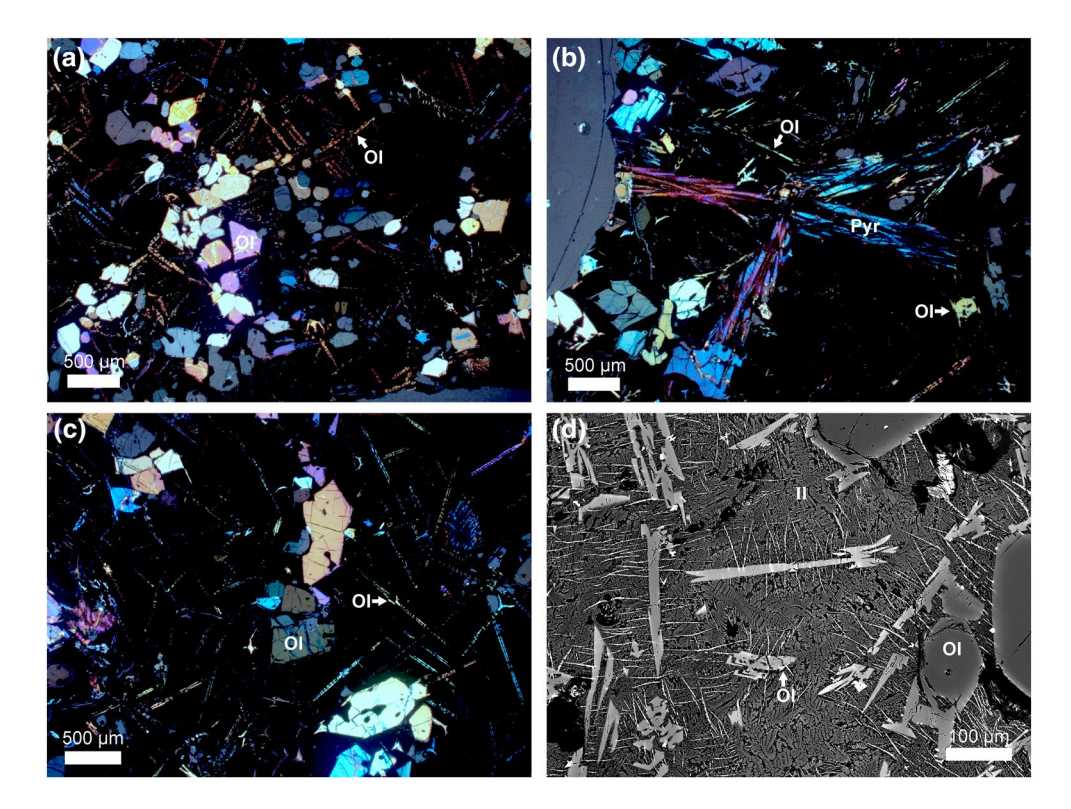


Figure 1. Petrographic microscope images of thin sections (a) 12008,41, (b) 12009,11, and (c) 12015,43, in transmitted light with crossed polarizers (scale bars 500 μ m), and (d) electron microprobe backscatter (BSE) image of thick section 12008,72hT (scale bar 100 μ m). Ol, olivine; Pyr, pyroxene; Il, ilmenite.

STRAUSS ET AL. 8 of 21

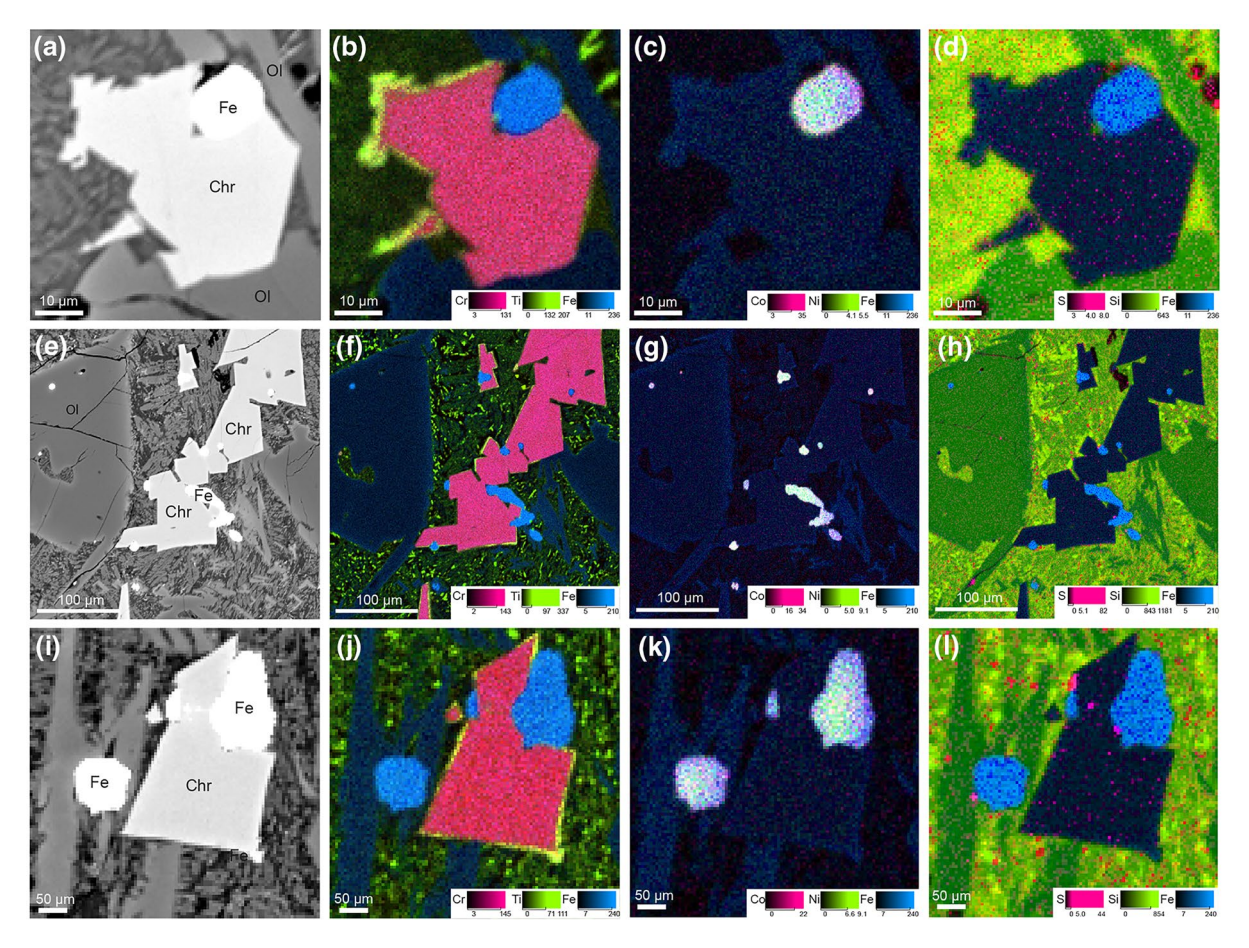


Figure 2. Microprobe images of representative regions from thin sections 12008,41 (a–d), 12009,11 (e–h), and 12015,43 (i–l). Leftmost column shows backscatter (BSE) images with mineral labels: Ol, olivine; Chr, chromite; Fe, iron-rich grain. Elemental maps show relative abundances of Cr, Ti, Fe (second column); Co, Ni, Fe (third column); S, Si, Fe (rightmost column).

are submicrometer metallic grains too small for targeted WDS analysis, consistent with magnetic results indicating the presence of even finer-grained ferromagnetic material (see Section 3.3). These results refine those provided by previous microscopic and electron microprobe studies that identified the metallic grains in 12008, 12009, and 12015 as iron (Brett et al., 1971; Dungan & Brown, 1977).

Sample 12015 was initially reported as a shocked basalt scoria due to both fracturing of the bulk sample and fractures observed microscopically in olivine phenocrysts (Warner, 1970). However, petrographic microscopy of thin sections shows that these irregular fractures are restricted to the olivine phenocrysts and are not present in other phenocrysts or groundmass. Although extremely weak undulatory extinction is visible in some olivine grains, suggesting that they experienced shock pressures between 4 and 15 GPa, there is no evidence for other post-formation shock features like mosaicism in either olivine or (ortho)pyroxene phenocrysts in any of the three samples, limiting the maximum pressure experienced by the sample after the formation of orthopyroxene to \approx 5 GPa (Stöffler et al., 2006).

3.2. ³⁹Ar/⁴⁰Ar Ages

Many, but not all, of the 20 aliquots from 12008, 12009, and 12015 show some degree of disturbance; however, all but two produced plateau ages (Table 4). The calculated $^{39}\text{Ar}/^{40}\text{Ar}$ plateau ages and associated 1σ error for the samples investigated, determined by variance weight average across aliquots, are 3065 ± 9 Ma (12008, 31 total steps), 3163 ± 5 Ma (12009, 62 total steps), and 3169 ± 4 Ma (12015, 157 total steps). Representative $^{39}\text{Ar}/^{40}\text{Ar}$ plateaus, K/Ca ratios, and isochron diagrams for each sample are presented in Figure 3. The same figures for each individual aliquot are located in the supplementary material (Figures S1–S3). Plateau ages

STRAUSS ET AL. 9 of 21



Table 3Representative Elemental Abundances of 12008,41, 12009,11, and 12015,43 Metal Grains Measured by Electron Microprobe (Full Results in Table S3)

				Sample	pple					
	12008,41				12009,11	L	12015,43			
Metal (mass %)	3,1,1	5,1,1	6,1,1	3,1,1	6,2,1	10,1,1	4,1,1	5,1,1	6,1,1	
S	0.01	0.01	0.52	0.01	0.01	0.01	0.01	0.01	0.01	
P	0.01	0.01	0.02	0.04	0.01	0.01	0.02	0.00	0.02	
Si	0.00	0.00	0.00	0.02	0.00	0.00	0.00	0.00	0.00	
Ti	0.09	0.17	0.07	0.13	0.15	0.03	0.11	0.04	0.07	
Al	0.00	0.02	0.01	0.10	0.37	0.22	0.17	0.10	0.19	
Cr	0.29	0.50	0.10	0.53	1.05	0.00	1.39	0.41	0.46	
Ca	0.12	0.15	0.08	0.18	0.14	0.05	0.08	0.04	0.06	
Mg	0.01	0.01	0.01	0.00	0.01	0.01	0.00	0.01	0.02	
Fe	90.02	85.98	84.98	92.10	80.65	77.57	81.98	79.68	79.97	
Mn	0.03	0.01	0.01	0.01	0.02	0.01	0.03	0.00	0.02	
Ni	9.70	12.23	11.87	4.59	15.21	20.18	17.11	18.37	17.64	
Co	1.24	1.18	1.39	1.13	1.19	1.20	1.05	1.40	1.25	
K	0.00	0.04	0.00	0.03	0.04	0.06	0.04	0.00	0.05	
Na	0.03	0.01	0.02	0.02	0.00	0.07	0.03	0.06	0.06	
Total	101.57	100.30	99.07	98.90	98.86	99.41	102.02	100.13	99.82	

Note. Locator strings (italics) list map, grain, shot for three shots from each sample.

were calculated assuming a nebular 40 Ar/ 36 Ar value of $<1 \times 10^{-5}$ (Clayton, 1977) for the trapped component. The plateau ages of all samples are defined steps ranging from 3 to 17 in number and make up >67% of the total 39 Ar_K released (Figure 3). In 11 of 18 aliquots with plateau ages, the plateau ages are older than the integrated (total fusion) ages, consistent with variable amounts of 40 Ar* loss from the sample, resulting in young apparent ages for low temperature gas extractions during step-heating experiments. In the remaining seven aliquots, integrated (total fusion) ages are older than corresponding plateau ages. For 4 of the 7 aliquots, the integrated and plateau ages are indistinguishable at the alpha-95% confidence interval. The older integrated ages for the remaining 3 aliquots can be explained by ingrowth of terrestrial excess 40 Ar, potentially during low-temperature weathering on Earth (e.g., Udry et al., 2019).

The measured atomic K/Ca ratio of the plateau steps varies from ≈ 0.005 to 0.027 for 12008, ≈ 0.003 to 0.045 for 12009, and ≈ 0.0006 to 4.692 for 12015 over the course of the experiments as different Ar reservoirs are sampled (Figure 3, Figures S1–S3). This indicates that K (39 Ar) and Ca (37 Ar) concentrations are not homogeneously distributed within the samples at mid-to high-release temperatures, likely an artifact of compositional variations within a single micro-milled sample. Within plateaus, however, 39 Ar and 40 Ar* concentrations are generally homogeneous despite variations in the atomic K/Ca ratio, and suggest a coeval closure of the Ar-system within this portion of the analyzed sample.

The slopes of the 40 Ar/ 36 Ar versus 39 Ar/ 36 Ar isochron ages correspond to an age of 3299 \pm 70 Ma for 12008, 3214 \pm 49 Ma for 12009, and 3152 \pm 29 Ma for 12015, calculated across all steps. For some of the aliquots analyzed, initial steps do not lie on the linear array defined by the remaining steps, again indicating potential ingrowth of a terrestrial 40 Ar/ 36 Ar signature. Overall, isochrons calculated for the 18 plateau-producing aliquots match well with the calculated plateau age from the same aliquot. All but two of the plateau-producing aliquots have isochron and plateau ages that are consistent at the alpha-95% confidence level. All dating results are included in the supplemental information as Tables S1 and S8 through S28, following the reporting guidelines of Renne et al. (2009).

STRAUSS ET AL. 10 of 21



Table 4Summary of ⁴⁰Ar/³⁹Ar Ages for Individual Aliquots From Samples 12008, 12009, and 12015

	Plateau					Isochron		Integrated				
Sample	Age (Ma)	±1σ	MSWD	n steps	K/Ca (×10 ⁻³)	±1σ	Age (Ma)	±1σ	Age (Ma)	±1σ	⁴⁰ Ar*/ ³⁹ Ar _K	±1σ
12008-03	3138	15	0.9	8	48.62	0.69	2989	220	3130	19	219.7	2.9
12008-04	3005	18	1.4	9	59.26	0.84	3073	84	3081	23	211.2	3.3
12008-05	3033	15	2.2	6	69.95	0.73	3650	611	3105	15	215.4	2.2
12009-01	3211	59	0.9	7	52.83	2.25	2943	230	3034	74	205.4	10.3
12009-02	3118	25	0.7	9	52.58	1.38	3152	200	3033	40	205.2	5.6
12009-03	3166.5	8.2	2.4	6	65.62	0.96	3347	57	3189	11	227.9	1.7
12009-04A	3164.8	7.5	1	8	60.67	0.61	3131	57	3255	14	238.3	2.2
12009-04B	3078	54	1.4	8	49.03	2.03	2784	230	3078	68	211.5	9.7
12015-01A	No Plateau						3425	291	2992	16	199.6	2.2
12015-01B	3196	29	1.1	10	77	1.85	2953	130	3156	36	223	5.4
12015-01C	3186.5	6.6	1.1	4	73.77	0.55	3296	66	3162	11	223.9	1.6
12015-02	3153	10	1.5	11	52.63	0.69	3128	31	3170	12	225.1	1.8
12015-03	3157.6	8.1	1.2	9	63.37	0.41	3234	42	3146.6	9.7	221.6	1.4
12015-04A	3022	61	0	3	47.21	2.24	8024	1203	3480	95	276.1	17
12015-04B	3110	38	0.7	11	68.23	2.52	2625	170	2976	63	197.5	8.6
12015-05A	3074	130	0.3	6	75.12	8.85	2747	541	2342	120	125.2	11.7
12015-05B	3094	120	0.9	10	31.57	3.83	3671	271	2773	110	171.6	13.9
12015-06	No Plateau						-2454	2980	1685	69	72.6	4.5
12015-07	3244	54	1.2	6	68.98	2.85	2745	280	2946	87	193.4	11.5
12015-0X	3201	52	0.2	11	78.19	4.11	3959	501	3066	91	209.9	13

Abbreviation: MSWD, mean square of weighted deviates.

3.3. Magnetic Characterization

Diamagnetic and paramagnetic contributions dominated hysteresis loops for all subsamples, likely due to the small grains used for analysis (Figure S4). Ferromagnetic contributions showed open loops suggestive of MD grain states, though they may also be explained by a combination of extremely weak samples and thermal disequilibrium of the AGFM. Bulk parameters were similar across samples, with coercivity (H_c) ranging from ≈ 5 to 9 mT and coercivity of remanence (H_{cr}) ranging from ≈ 27 to 41 mT. Saturation remanent magnetization (M_r) and saturation magnetization (M_s) ranged between $\approx 10^{-5}-10^{-3}$ Am²/kg and $\approx 10^{-6}-10^{-4}$ Am²/kg, respectively. Mean values for hysteresis parameters are reported in Table S4.

3.4. Paleomagnetism

The results of AF demagnetization are summarized in Table S5 and Figure S5. NRM values for subsamples from 12008 (Figure 4a) range in intensity between $\approx 6 \times 10^{-7}$ Am²/kg and $\approx 2 \times 10^{-5}$ Am²/kg. Four subsamples show a low-coercivity (LC) component of magnetization blocked up to ≈ 10 mT, while the fifth (subsample e) has an LC component blocked up to ≈ 58 mT. Subsequent to the removal of this LC component, some subsamples show multiple unstable mid-coercivity components; after these mid-coercivity components are removed, remaining high-coercivity (HC) magnetization is indistinguishable from noise. We found that principal component analysis (PCA) fits of the HC noise directions of all five subsamples exhibit different orientations (angular offsets range from 28.5° to 140.7°, $\kappa = 1.53$, $\alpha_{95} = 50.57$. κ is a precision parameter indicating how concentrated the distribution is around the true mean direction, α_{95} is the calculated confidence limit) in spite of their mutual physical orientation. LC components pass a Watson conglomerate test (Watson, 1956), indicating that they may be randomly oriented (five subsamples used, $\kappa = 2.02$, $\alpha_{95} = 44.09$,

STRAUSS ET AL. 11 of 21

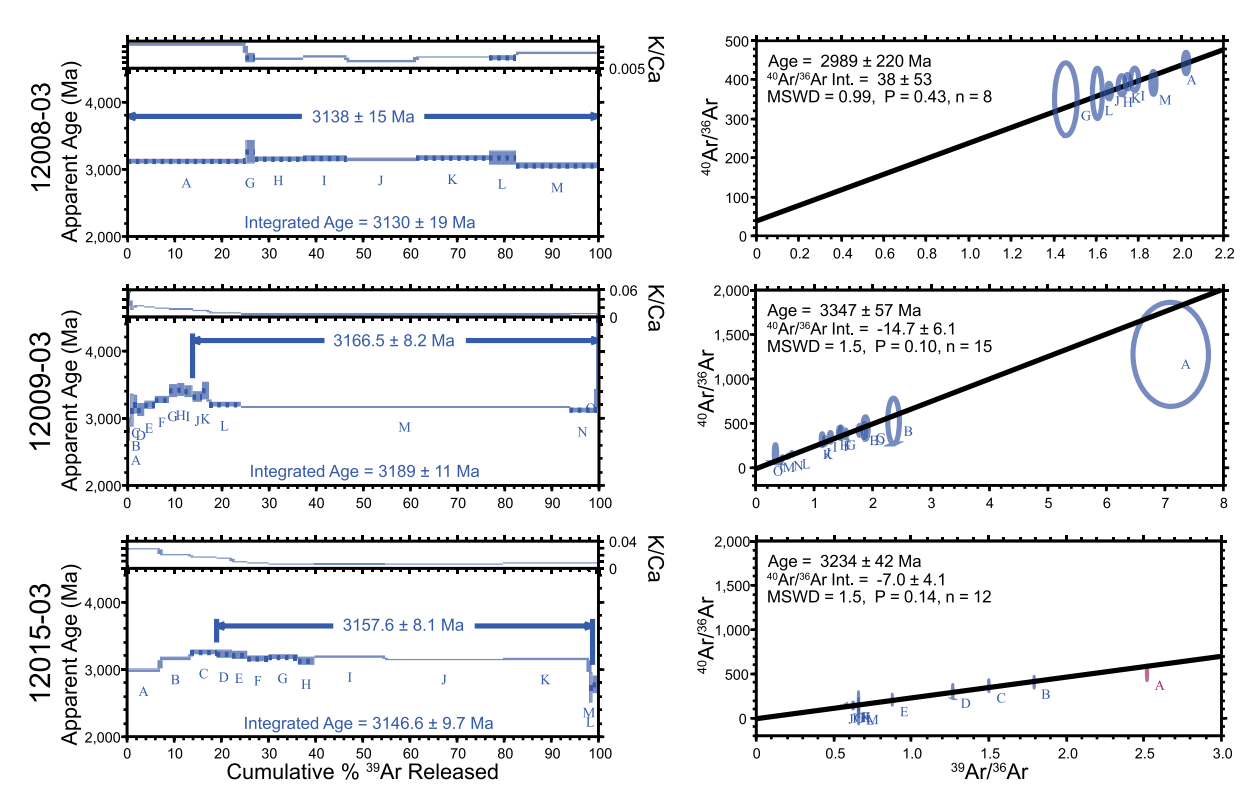


Figure 3. 40 Ar/ 39 Ar results for representative aliquots from samples 12008 (top), 12009 (middle), and 12015 (bottom). (Left) Step-heating age spectra and K/Ca ratios. (Right) Isochron correlation diagrams. Error ellipses, calculated ages, and initial 40 Ar/ 36 Ar values are displayed with 1σ uncertainties.

 $R = 2.39 < R_0 = 3.50$ for 95% confidence. R is the resultant vector of the addition of unit vectors, and R_0 is a critical value below which results are likely to come from a random population). Possible anisotropy-driven pinning of remanence was observed in subsamples e, f, and g. Subsamples e and f both show LC (<50 mT)

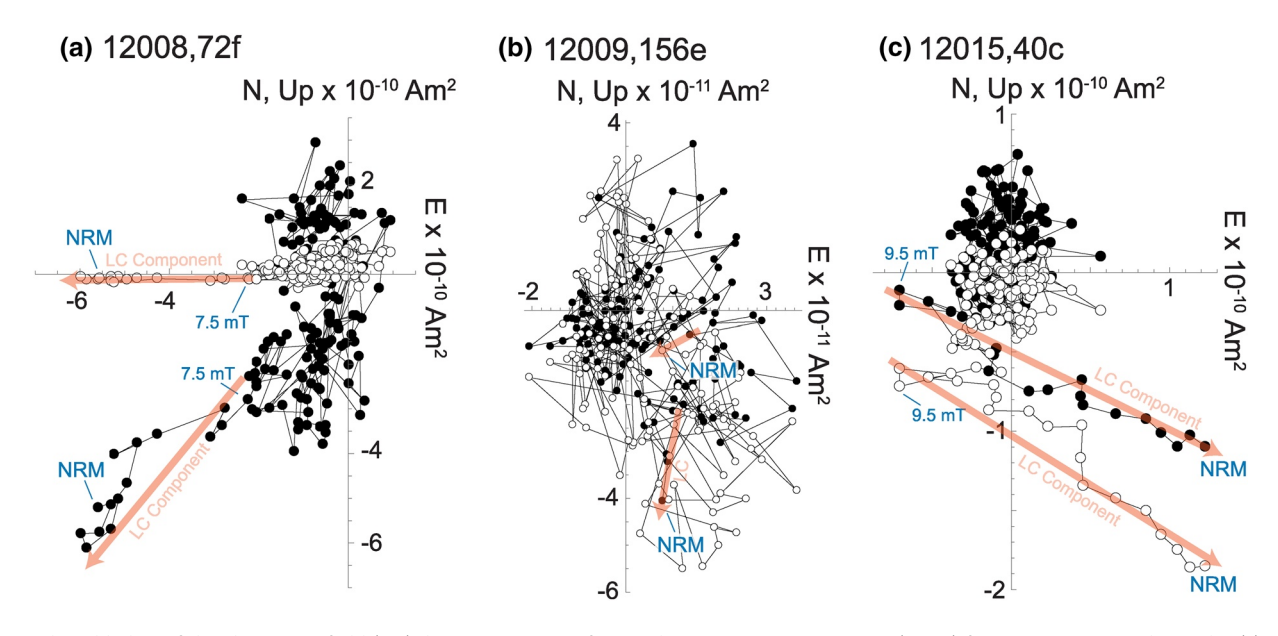


Figure 4. Zijderveld plots of the alternating field (AF) demagnetization of natural remanent magnetization (NRM) for representative subsamples (a) 12008,72f, (b) 12009,156e, and (c) 12015,40c. Closed circles represent end points of magnetization projected on the horizontal (N and E plane. Open circles represent end points of magnetization projected on vertical (Up and E) plane. Peak fields for selected AF steps are labeled in mT in blue. Low-coercivity (LC) magnetization components are labeled and represented with pale orange arrows.

STRAUSS ET AL. 12 of 21



remanence clusters oriented $\approx 130^\circ$ to 150° apart from higher-coercivity remanence clusters ($\approx 50-145$ mT), while subsample g displays magnetic pinning comparable to that described by Tikoo et al. (2012) as "spectacular" in subsample 15556,221c, a fine-grained Apollo 15 basalt. Subsamples c and d show no evidence of pinning.

Subsamples from 12009 (Figure 4b) have NRM values of $\approx 1 \times 10^{-7}$ Am²/kg to $\approx 3 \times 10^{-6}$ Am²/kg, an order of magnitude weaker than those from 12008. AF demagnetization reveals a low-coercivity component blocked up to ≈ 4 -8 mT in three subsamples, with no clear LC component detectable in subsample h and no significant components detectable in subsample f. LC components for subsamples c-e and initial components for subsamples f and h pass a Watson conglomerate test and may therefore be randomly oriented (five subsamples used, $\kappa = 1.40$, $\alpha_{95} = 52.87$, $R = 1.19 < R_0 = 3.50$ for 95% confidence). The highest-coercivity magnetization within each subsample is unstable and these features are non-unidirectional between mutually oriented subsamples (offset range 29.0° to 145.4°, $\kappa = 1.05$, $\alpha_{95} = 61.08$); no stable high-coercivity magnetization (i.e., primary remanence) was retrieved from any of the five subsamples.

NRM values for subsamples from 12015 (Figure 4c) were intermediary relative to those from 12008 and 12009, ranging from \approx 7 × 10⁻⁷ Am²/kg to \approx 5 × 10⁻⁶ Am²/kg. Four of the five subsamples showed a semi-linear LC component blocked up to \approx 10–20 mT, while the LC component detected in subsample h was removed by 3.5 mT. LC components pass a Watson conglomerate test and may be randomly oriented (5 subsamples used, $\kappa = 1.29$, $\alpha_{95} = 55.13$, $R = 0.633 < R_0 = 3.50$ for 95% confidence). As in samples 12008 and 12009, the highest-coercivity remanence is unstable and non-unidirectional between mutually oriented subsamples (offset range 31.6° to 160.1°, $\kappa = 0.92$, $\alpha_{95} = 65.42$).

To quantitatively assess whether the highest-coercivity magnetizations measured were origin-trending, we compared MAD with deviation angle (DANG), the angle between the centroid of the PCA fit and the fit's direction without forcing through the origin. If MAD is greater than DANG, the fit direction trends toward the origin (Tauxe & Staudigel, 2004). HC directions were not origin-trending for any of the 15 subsamples (Table S5, Figure S5). No stable, internally consistent high-coercivity magnetization was retrieved from any of the subsamples analyzed.

3.4.1. Viscous Remanent Magnetization

The decay rate of the laboratory VRM (Figure S6) acquired in \approx 1 week by sample 12015 was approximately linear with log (time) ($R^2 = 0.923$), enabling us to calculate a magnetic viscosity decay coefficient S_d :

$$S_{\rm d} = \frac{d({\rm VRMlost})}{d\log({\rm time})} \tag{2}$$

of 7.17×10^{-12} Am²/log(s). By extrapolating the linear fit to our experimental data from 1 week to 48 years (43 in the Earth's field, 5 in magnetically shielded rooms), we can provide an estimate for how much of the NRM in 12015 can be accounted for by VRM. In this case, the total VRM resulting from 43 years of exposure to the Earth's magnetic field, followed by five years of storage in magnetically shielded rooms, would be $\approx 7\%$ of the total NRM. The decay rates of the laboratory VRM in samples 12008 and 12009 were best, albeit poorly, expressed as exponential with log (time) ($R^2 = 0.849$ and 0.805 respectively). In both cases, the total VRM after 48 years would account for <0.1% of the total NRM. Uncertainties in these estimates are due to the use of specimens that were AF demagnetized prior to VRM acquisition, which can result in underestimation of VRM intensity (Lowrie & Kent, 1978), and to these calculations' incorrect assumption that the samples remained stationary throughout their exposure to the Earth's field at JSC when in fact the parent chips were physically manipulated during the processes of routine subdivision and storage.

3.5. Paleointensity

The results of our paleointensity fidelity limit experiments are reported in Table S6 and Figure S7, while the relationship between the applied TRM-equivalent laboratory field and the retrieved paleointensity for each sample is shown in Figure 5. The magnetic fidelity of a sample was considered acceptable if the difference between the retrieved paleointensity and the laboratory field was less than a factor of 2 and associated error was less than 100% (i.e., the width of the 95% confidence interval, or the formal uncertainty, of the retrieved

STRAUSS ET AL. 13 of 21

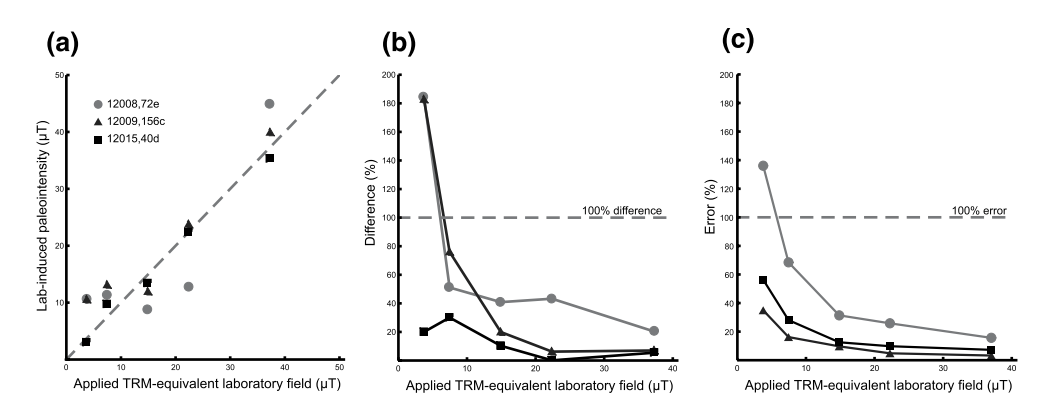


Figure 5. Paleointensity fidelity limit tests. (a) Recovered lab-induced paleointensities versus TRM-equivalent applied laboratory field for 12008,72e (light gray circles), 12009,156c (dark gray triangles), and 12015,40d (black squares). Gray dashed line indicates 1:1 relationship. (b) Percentage difference for retrieved paleointensities versus applied laboratory field by sample. Dashed horizontal line marks the threshold of 100% difference between the applied field and the retrieved paleointensity. (c) Error for retrieved paleointensities versus applied laboratory field by sample. Dashed horizontal line marks the threshold of 100% error.

paleointensity value is equal in magnitude to the applied TRM-equivalent laboratory field) following Tikoo et al. (2012); Tikoo et al. (2014).

For both subsample 12008,72e and subsample 12009,156c, we found poor correspondence between expected and retrieved paleointensities below $\approx 7~\mu T$, while for subsample 12015,40d, we found poor correspondence below $\approx 4~\mu T$. Thus, AF methods should be capable of retrieving stable TRM records acquired in paleofields $> \approx 7~\mu T$ from samples 12008 and 12009, and those acquired in paleofields $> \approx 4~\mu T$ from sample 12015.

4. Discussion

4.1. Mineralogy and Cooling History

Samples 12008, 12009, and 12015 are among the most rapidly cooled of the Apollo 12 basalts (Dungan & Brown, 1977; Rhodes et al., 1977). The skeletal olivine phenocrysts, characterized in all three samples by elaborate cross-ornamentation, were likely first to form, accompanied by an initial population of Fe-Ni grains and angular chromite phenocrysts. Cooling experiments of a picrite basalt with a similar composition to 12009 found that cooling rates greater than 500 °C/h produced olivine with similar skeletal textures, while cooling rates greater than 10^5 °C/h produced glass with no olivine crystals (Walker et al., 1976). The presence of these textures in samples 12008, 12009, and 12015 (Figure 1) suggests that all three samples experienced initial cooling rates between ≈ 500 °C/h and 10^5 °C/h, constraining their cooling times from melt to crystallization to <2 h. Additional Fe-Ni grains formed floating in the matrix prior to very rapid quenching, suggested by the dendritic texture of the melt and the presence of immiscible submicrometer oxide grains.

The lack of post-formation shock features indicates that these samples were not subject to high (>4–15 GPa) pressures after formation and are unlikely to have acquired shock remanent magnetization (SRM). Because these samples are vitrophyric basalts formed by rapid cooling from lava, the most likely mechanism of initial remanence acquisition for all three samples is thermal in origin, with kamacite grains acquiring TRM during primary cooling. Although metal with higher Ni contents would initially have formed taenite during cooling, this taenite would have transformed to martensite between 200 °C and 500 °C, depending on Ni content (Swartzendruber et al., 1991; Uehara et al., 2011). Upon this transformation, martensite grains would have been close to their Curie temperatures and thus should have largely acquired TRM as well.

4.2. Paleomagnetism

AF demagnetization does not reveal any stable high-coercivity component of NRM in any subsamples from samples 12008, 12009, or 12015. Rather, after the removal of an initial low-coercivity component from all

STRAUSS ET AL. 14 of 21

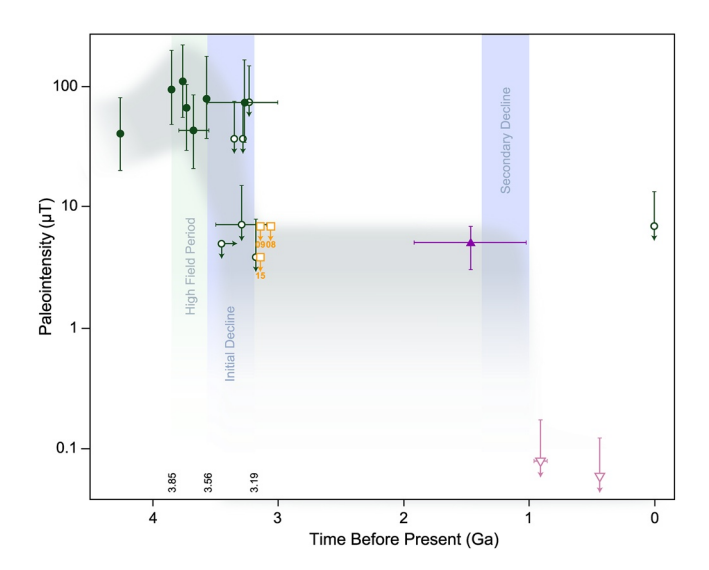


Figure 6. Paleointensity measurements of the lunar magnetic field as a function of time. Each point represents a paleointensity measurement from an individual Apollo sample. Closed points represent actual paleointensities; open points represent upper limits on paleointensity. Each point is located at the given average from its source study, with error bars derived from each individual study; right-pointing (downward-pointing) arrows represent upper limits on age (paleointensity). When not shown, error bars for ages are within point size (<0.05 Ga). Green circles are re-plotted from Weiss and Tikoo (2014), purple triangle represents data from Tikoo et al. (2017) with updated age range from Mighani et al. (2020), pink inverted triangles represent data from Mighani et al. (2020) (ARM paleointensity fidelity limits shown), and orange squares represent data from this study. Gray envelope illustrates the the trajectory of field decline.

but one subsample, the remaining magnetization is either consistent with pinning behavior or non-resolvable as a trending component. Although LC components from several subsamples meet a mean angular deviation (MAD) cutoff of $\leq 15^{\circ}$ (Tauxe & Staudigel, 2004), no higher-coercivity components pass that cutoff, except for subsample 12008,72g, which exhibits dramatic zig-zag magnetization indicating likely textural remanence.

The LC components are likely overprints acquired subsequent to initial rock formation and cooling. Chemical remanent magnetization (CRM) may be ruled out as a source of magnetization due to the lack of aqueous alteration on the Moon. The acquisition of semi-linear overprints removed by fields ≤58 mT must therefore be attributed to some other mechanism of remagnetization. The results of our laboratory VRM experiments indicate that in comparison to sample 15498 (Tikoo et al., 2017), all three Apollo 12 samples described in this study are highly resistant to remagnetization by VRM. Furthermore, these three samples were stored in magnetically shielded rooms for an extended period of time (five years) prior to measurement. This combination suggests that the measured NRMs of these samples cannot be readily explained by VRM acquired in Earth-strength fields, although it is possible that our use of previously AF demagnetized samples produced underestimates of VRM intensity (Lowrie & Kent, 1978). The low-coercivity overprints found in some sample are broadly consistent with secondary IRM components observed in other lunar samples (Figure S5), though these are typically unblocked by 10 mT (Fuller et al., 1979; Tikoo et al., 2017). One possible explanation for these overprints is the acquisition of weak IRM during flight in the Apollo spacecraft (NASA Manned Spacecraft Center, 1972; Strangway et al., 1973). Alternatively, multiple grain size populations may have different VRM acquisition efficiencies, and compositional variations across parent chips may therefore produce differing VRM acquisi-

tion rates between subsamples, which could allow for the presence of VRM-induced LC overprints in some but not all subsamples.

4.3. The Lunar Paleofield at ≈3.1 to 3.4 Ga

Our results from samples 12008, 12009, and 12015 replicate the \approx 7 μ T paleointensity fidelity threshold found by previous work on lunar materials with similar grain sizes, particularly sample 15597, a rapidly cooled vitrophyric pigeonite basalt (Tikoo et al., 2014), and the glass spatter coating sample 12017 (Buz et al., 2015). Such glassy rocks provide somewhat more restrictive paleointensity constraints than more crystalline basalts (e.g., \approx 37 μ T for the porphyritic basalt portion of sample 12017 [Buz et al., 2015; Tikoo et al., 2014] and medium-grained basalt 15016 [Tikoo et al., 2012], \approx 75 μ T for fine-grained basalt sample 15556 [Tikoo et al., 2012]).

These results suggest that at ≈ 3.1 Ga, lunar magnetic fields were no longer strong enough to impart magnetizations retrievable by AF methods to our samples (Figure 6). In combination, the lack of stable, high-coercivity magnetization and the low paleointensity field limits ($\approx 4-7~\mu T$) in samples 12008, 12009, and 12015 indicate that all three rocks likely formed (cooled from melt through their blocking temperatures) in weak to null paleofield. This proposed upper limit is consistent with recent studies of lunar mare basalts of similar ages, indicating a weak lunar paleofield between 3.4 and 3.1 Ga (Buz et al., 2015; Lawrence et al., 2008; Tikoo et al., 2014). We therefore find no evidence for lunar surface fields $> \approx 7~\mu T$ at ≈ 3.1 Ga.

4.3.1. Constraining the Decline in Lunar Paleointensities

To determine whether the observed decline in lunar paleointensities after 3.56 Ga is statistically significant, we use the Kolmogorov-Smirnov (K-S) statistical test after Tikoo et al. (2014). By comparing the lunar paleo-

STRAUSS ET AL. 15 of 21



intensities of samples from the previously established high field period (>3.56 Ga) with younger samples from the initial era of field decline (\approx 3.1–3.56 Ga), we can assess the null hypothesis that these values are derived from the same distribution of paleointensity values at the 5% significance value (p). Average paleointensities and paleointensity fidelity limits from previous studies are reported in Table 1, which includes seven samples older than 3.56 Ga and six samples from the period \approx 3.1 to 3.56 Ga, in addition to the three samples analyzed in this study. (Samples younger than 3.1 Ga are excluded from this calculation.) Prior to this study, the null hypothesis could be rejected with a p-value of 0.0152. With the addition of the paleointensity fidelity limits from samples 12008, 12009, and 12015, we improve this p-value to 0.0014 (>95% confidence).

Most of the paleointensities and paleointensity fidelity limits used in this analysis were developed using f'=1.34, a value originally calibrated for kamacite (see Section 2.5); however, we note that while the Apollo 11 and 17 basalt samples formed during the high field epoch have generally lower Ni content consistent with kamacite, younger Apollo 12 and 15 basalts often have higher Ni contents more consistent with martensite. Although these two minerals have similar overall magnetic properties (Kletetschka & Wieczorek, 2017; Wasilewski, 1974), we explore whether the two distributions of paleointensities described here are truly distinct by repeating the K-S test while varying f' by a factor of 2 for the younger martensite-bearing samples. In cases where f'=0.68, the K-S test returns a p-value of 0.0000874, while in cases where f'=0.67, the resulting p-value is 0.0283, enabling definitive rejection of the null hypothesis that both datasets are from the same distribution despite uncertainty in their associated material properties. We can therefore confidently state that the pre-3.56 Ga paleointensities are distinct from the post-3.56 Ga upper paleointensity limits, and that the significant decline in the intensity of lunar surface fields between 3.56 Ga and 3.1 Ga described by previous studies is indeed genuine.

4.4. Implications of a Paleointensity Decline

The decrease in lunar paleointensities from ≈77 µT at 3.56 Ga (Weiss & Tikoo, 2014) to < ≈7 µT by 3.19 Ga (Suavet et al., 2013; Tikoo et al., 2014), a field intensity drop of an order of magnitude in ≈370 Ma, can only be explained by a rapidly declining dynamo. The constraints provided by samples 12008, 12009, and 12015 are consistent with previously published work (Table 1) and contribute robust evidence that this decline is not the product of small number statistics, but rather is genuine. The abrupt shift from the high field period to the low field period can be explained in one of two ways: either the dynamo was powered by a single bistable mechanism that changed state between ≈3.56 and 3.19 Ga, or (at least) two distinct mechanisms are responsible for the two field intensity epochs. None of the dynamo generation mechanisms proposed previously and described above have been shown to accurately reproduce the two-stage field intensity record (Tikoo et al., 2017). At present, a two-mechanism scenario is best explained by initial mantle precession, which could have produced ≈10-100 µT fields consistent with the high field period until ≈3.56 Ga (Dwyer et al., 2011; Stanley et al., 2017) but would have been unlikely to sustain such fields beyond ≈2 Ga due to the increasing distance between the Moon and the Earth (Tikoo et al., 2014; Weiss & Tikoo, 2014). Upon the decline of this precession-generated dynamo, a second mechanism would be required to account for the sustained low field period. Two possible candidates are thermochemical convection produced by core crystallization, suggested by thermal evolution models to be capable of generating ≈1 µT surface fields through ≈1 Ga (Laneuville et al., 2014; Mighani et al., 2020; Scheinberg et al., 2015; Zhang et al., 2013), and inner core precession driving viscous friction, which could sustain ≈1–5 μT surface fields for a similar length of time (Stys & Dumberry, 2020).

4.5. The Role of Mineralogy in Paleomagnetic Fidelity

The magnetic recording capabilities of Apollo material vary widely, with reported paleointensity thresholds ranging from \approx 4 to \approx 75 μT (Table 1). Due to the diversity of lunar materials studied, this range in fidelity limits has been attributed to a variety of sources, including magnetic anisotropy, composition, and grain size.

Another possible explanation is the distribution of magnetic grains with respect to non-magnetic matrix minerals and other grains. Previous work on lunar vitrophyre 15597, a high-fidelity magnetic recorder

STRAUSS ET AL. 16 of 21



(paleointensity fidelity limit $\approx 7~\mu T$), categorized constituent kamacite and martensite in three groups: (1) solitary irregularly shaped $\approx 5-20~\mu m$ inclusions in pyroxene, (2) associations of $\approx 1-20~\mu m$ grains with chromite in pyroxenes, and (3) $\approx 10~\mu m$ grains in the mesostasis glass (Fuller, 1974; Tikoo et al., 2014). $\approx 1-20~\mu m$ Fe-Ni grains were also found in association with chromite in sample 12022 (Tikoo et al., 2014). In samples 12008, 12009, and 12015, micrometer-scale kamacite grains were most commonly found in association with chromite (Figure 2), though several were found as inclusions in olivine phenocrysts (Figures 2e-2h) or solitary grains in the mesostasis glass (Figures 2i-2l).

We also explore the possibility that Fe-Ni textural associations with troilite may serve as indicators of pale-omagnetic fidelity in lunar basalts. Submicrometer grains of low-Ni (<1 mass %) kamacite within large (>10 μm) troilite grains have been identified in Apollo 11 sample 10020, which has a reported paleointensity fidelity threshold of \approx 7 μT (Shea et al., 2012), as well as in samples 10017 and 10049 (Suavet et al., 2013). Warner (1970) reported abundant troilite in Apollo 12 samples, but noted that unlike in the Apollo 11 rocks, visible metallic iron grains in these samples are often larger (1–30 μm in diameter) and are not typically associated with that troilite. However, it should be noted that similarly sized (5–30 μm) kamacite grains were adjacent to troilite in sample 12022, one of the highest-fidelity lunar samples on record with a reported fidelity limit of \approx 4 μT (Tikoo et al., 2014). Tikoo et al. (2012) found small (<5 μm) low-Ni (<1 mass %) kamacite adjacent to troilite in samples 15556, 15016, and the basalt portion of 12017, all three of which have relatively poor magnetic fidelity thresholds (Tikoo et al., 2014). The samples in this study confirm that although the processes that produce troilite during cooling may also produce submicrometer iron grains, the intergrowth of kamacite with troilite is not a requirement for high paleointensity fidelity, and that petrographic studies aimed at identifying high-fidelity samples should therefore prioritize submicrometer Fe-Ni grains in general.

Here, we consider the role of the fine kamacite grain size observed in multiple high-fidelity samples. The distribution of magnetic grain sizes (i.e., domain states) is a major control on magnetic fidelity; large multidomain (MD) grains have non-uniform magnetization that complicates their ferromagnetic behavior, while smaller grains with a single domain (SD) behave more predictably and are expected to hold records of magnetizing fields for billions of years. Tikoo et al. (2012) attributed the unreliable remanence behavior of lunar basalts 12017, 15016, and 15556 in part to their relatively high fractions of MD grains compared to mare basalts with more readily retrieved paleointensities (e.g., Cournède et al., 2012; Shea et al., 2012; Suavet et al., 2013). Meanwhile, the glass spatter portion of sample 12017, analyzed by Buz et al. (2015), is described as MD but is a relatively high-fidelity paleorecorder, with a reported fidelity threshold of $\approx 7 \,\mu\text{T}$. Work on other extraterrestrial materials has also shown that MD grains are capable of carrying stable remanence (Garrick-Bethell & Weiss, 2010; Gattacceca et al., 2014; Suavet et al., 2014), possibly due to domain pinning (Lindquist et al., 2015). The dominant carriers of remanent magnetization in lunar materials are iron metal and iron alloys with nickel, cobalt, and other trace contaminants (Fuller, 1974; Garrick-Bethell & Weiss, 2010). Kamacite, martensite, and metallic iron were identified as the carriers of magnetization for all samples described in Table 1. However, no critical grain size thresholds for these magnetic minerals (particularly kamacite) have been defined quantitatively. Further, recent work in terrestrial micromagnetics has shown that the domain size model itself may be an oversimplification (see Roberts et al., 2017, and others).

We propose that a Day plot (Day et al., 1977) may be used to compare the magnetic properties of various samples, without ascribing strict "grain size" parameters to individual samples based on their bulk magnetic behavior (see Cournède et al., 2012; Mighani et al., 2020). In such a plot, the remanent coercivity (H_{cr}) divided by the coercive force (H_c) for a given sample is plotted against the magnitude of the saturation remanent magnetization (M_r) divided by the magnitude of the saturation magnetization (M_s) for that sample. The Day plot is an imprecize metric for the assessment of magnetic grain sizes (Roberts et al., 2018) but may still be used as a general comparative tool for different populations of magnetic grains, as regardless of specific grain size, magnetic fidelity (a property traditionally associated with SD grains) is expected to increase with lower H_{cr}/H_c and higher M_r/M_s (toward the upper left in Figure 7).

To contextualize the results described above, we compared the magnetic analyses of our high-fidelity lunar basalts with previously published studies of other lunar material, enabling us to assess the diversity of magnetic characters among the Apollo sample suite. Figure 7 shows a modified Day plot in which the H_{cr}/H_c and M_r/M_s ratios for more than 80 Apollo rock and soil samples from previous studies (Table S7),

STRAUSS ET AL. 17 of 21

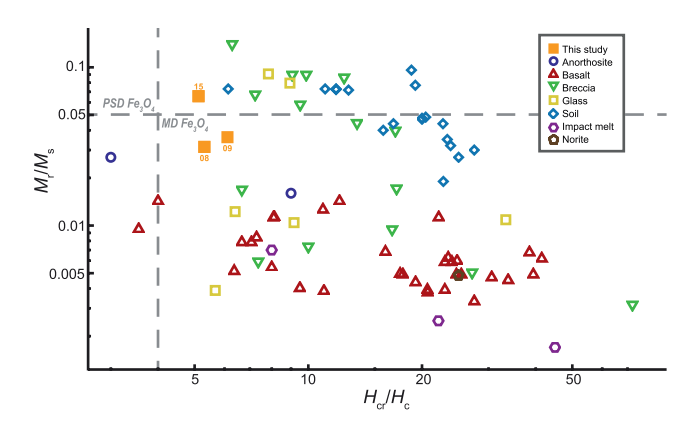


Figure 7. Day plot (Day et al., 1977) of hysteresis parameters for samples collected during the Apollo missions. The remanent coercivity ($H_{\rm cr}$) divided by the coercive force ($H_{\rm c}$) for each sample is plotted against the magnitude of the saturation remanent magnetization ($M_{\rm r}$) divided by the magnitude of the saturation magnetization ($M_{\rm s}$). Data from this study are shown as closed orange squares. Data from previous studies are plotted as open shapes by rock type and are also provided in Table S7. Regions indicating domain state (PSD, pseudo-single domain; MD, multidomain) determined for pure euhedral magnetite (Fe₃O₄) from Day et al. (1977) are provided in gray for reference but should not be used to interpret the domain states of the lunar samples shown here, as these regions are not yet defined for kamacite and martensite.

organized by rock type are plotted alongside averaged results of hysteresis experiments from this study (Table S4), and no grain size ranges are provided. (The domain state parameters often used as a proxy for magnetic grain size in magnetite, Fe_3O_4 , have not been defined for kamacite and martensite and should therefore not be used to assess the domain states of lunar samples. See Roberts et al. (2018) for extensive discussion of the problems with such approaches.)

Lunar basalts in previous studies have generally low M_r/M_s compared to other rock types, though their H_{cr}/H_c ratios cover almost the full range of reported values. These materials have a correspondingly broad range of paleomagnetic fidelities (Table 1, Figure 6). In comparison, the M_r / $M_{\rm s}$ ratios of lunar glasses range from relatively low values to some of the highest reported (e.g., Buz et al., 2015; Tikoo et al., 2017). Samples 12008, 12009, and 12015 show broadly lower H_{cr}/H_c and higher M_r/M_s ratios than most other lunar materials and are most comparable to lunar glasses in terms of both their overall grain size, determined through non-magnetic methods, and their hysteresis parameters, used here as an indicator of remanence behavior. This result is consistent with the presence of both submicrometer magnetic grains too small to be imaged readily and larger magnetic grains whose multidomain behavior could dominate simple hysteresis experiments. They are also similar to troctolite 76535, whose magnetic grains were reported to be pseudo-single domain in size (Garrick-Bethell et al., 2009).

Thus, iron mineral grain size (which is tied to domain state) appears to be the dominant controller of paleomagnetic fidelity. Future selection of

samples for paleomagnetic analysis based on petrologic type alone may not be useful and must also be informed by domain state considerations. These comparisons would be further enhanced through the use of first-order reversal curve (FORC) data; however, much of the existing lunar magnetism literature predates the development of FORC experiments (Pike et al., 1999; Roberts et al., 2000), and we therefore encourage the inclusion of FORCs in future studies of Apollo materials to improve both the differentiation of magnetic grain size populations in a given sample and the overall availability of domain state data.

5. Conclusions

Apollo samples 12008, 12009, and 12015 are vitrophyre mare basalts whose paleomagnetic remanence is likely held by small (submicrometer) Fe-Ni grains. The high paleomagnetic fidelities (\approx 4–7 μ T) of these samples are likely explained by the fine grain size of constituent magnetic minerals, but further work is required to develop a meaningful framework through which to interpret lunar magnetic mineralogy across rock types.

Despite their paleomagnetic fidelity properties, none of the three samples contain records of magnetic fields consistent with a strong lunar dynamo. The Moon's magnetic field must therefore have diminished to a surface intensity of <4–7 μT by the time these rocks cooled through their blocking temperatures $\approx 3.1–3.2$ Ga. This statistically robust timepoint helps to constrain the initial decline of the Moon's magnetic field to a 370-million-year window, after which it sustained a low field state for an additional one to two billion years. The rapid field decline described here is consistent with a change in field generation mechanism, which could be explained by either a single bistable mechanism or two distinct mechanisms operating during different stages of lunar history.

Data Availability Statement

Data from this study can be found in the references, tables, and supplemental information, and all data is available in the NIST Public Data Repository at https://doi.org/10.18434/mds2-2303, Strauss (2020).

STRAUSS ET AL. 18 of 21



Acknowledgments

We thank the Curation and Analysis Planning Team for Extraterrestrial Materials (CAPTEM) for sample allocation. Thank you to B. P. Weiss for use of the MIT Paleomagnetism Laboratory, T. C. Prissel for assistance with microprobe analyses, C. M. Mercer for assistance with isotopic data management, R. Fu for assistance with magnetic data plotting, M. Fuller for access to an unpublished compilation of magnetic characterization literature, and M. Jackson and P. Solheid of the Institute for Rock Magnetism for technical support. We thank reviewers C. Nichols and H. Wang for insightful comments that greatly improved this manuscript. Author BES received supplemental funding for this work through a National Research Council postdoctoral fellowship at the National Institute of Standards and Technology.

References

- Brett, R., Butler, P., Jr., Meyer, C., Jr., Reid, A. M., Takeda, H., & Williams, R. (1971). Apollo 12 igneous rocks 12004, 12008, 12009, and 12022: A mineralogical and petrological study (pp. 301–317). Proceedings of the 2nd Lunar Science Conference, Houston, TX.
- Buz, J., Weiss, B. P., Tikoo, S. M., Shuster, D. L., Gattacceca, J., & Grove, T. L. (2015). Magnetism of a very young lunar glass. Journal of Geophysical Research: Planets, 120, 1720–1735. https://doi.org/10.1002/2015JE004878
- Carr, M. J., Saginor, I., Alvarado, G. E., Bolge, L. L., Lindsay, F. N., Milidakis, K., et al. (2007). Element fluxes from the volcanic front of nicaragua and costa rica. Earth and Planetary Science Letters, 363, 50–60.
- Cisowski, S. M., & Fuller, M. (1986). Lunar paleointensities via the IRMs normalization method and the early magnetic history of the Moon. In W. K. Hartmann, R. J. Phillips, & G. J. Taylor (Eds.), *Origin of the moon* (pp. 411–424). Houston, TX: Lunar and Planetary Institute.
- Clayton, D. D. (1977). Interstellar potassium and argon. Earth and Planetary Science Letters, 36(3), 381-390.
- Cournède, C., Gattacceca, J., & Rochette, P. (2012). Magnetic study of large Apollo samples: Possible evidence for an ancient centered dipolar field on the Moon. Earth and Planetary Science Letters, 331–332, 31–42. https://doi.org/10.1016/j.epsl.2012.03.004
- Dalrymple, G. B., & Lanphere, M. A. (1969). In J. Gilluly & A. O. Woodford (Eds.), Potassium-argon dating: Principles, techniques and applications to geochronology. US: W. H. Freeman & Company. Retrieved from https://www.amazon.com/Potassium-Argon-Dating-Principles-Applications-Geochronology/dp/B0000EG5N3
- Dalrymple, G. B., & Lanphere, M. A. (1974). ⁴⁰Ar/³⁹Ar age spectra of some undisturbed terrestrial samples. *Geochemica et Cosmochimica Acta*, 38(5), 715–738.
- Day, R., Fuller, M., & Schmidt, V. A. (1977). Hysteresis properties of titanomagnetites: grain-size and compositional dependence. *Physics of the Earth and Planetary Interiors*, 13, 260–267.
- Donovan, J. J., Singer, J. W. S., & Armstrong, J. T. (2016). A new EPMA method for fast trace element analysis in simple matrices. *American Mineralogist*, 101(8), 1839–1853.
- Dungan, M. A., & Brown, R. W. (1977). The petrology of the Apollo 12 ilmenite basalt suite (Vol. 8, pp. 1339–1381). Proceedings of the Lunar and Planetary Science Conference, Houston, TX.
- Dunn, J. R., Fuller, M., & Clauter, D. A. (1981). On the estimation of lunar paleointensities—Studies of synthetic analogues of stably magnetized samples (Vol. 12b, pp. 1747–1758). Proceedings of the Lunar and Planetary Science Conference, Houston, TX.
- Dwyer, C. A., Stevenson, D. J., & Nimmo, F. (2011). A long-lived lunar dynamo driven by continuous mechanical stirring. *Nature*, 479, 212–214. https://doi.org/10.1038/nature10564
- Evans, A. J., Tikoo, S. M. T., & Andrews-Hanna, J. C. (2018). The case against an early lunar dynamo powered by core convection. *Geophysical Research Letters*, 45(1), 98–107. https://doi.org/10.1002/2017GL075441
- Evans, A. J., Zuber, M. T., Weiss, B. P., & Tikoo, S. M. (2014). A wet, heterogeneous lunar interior: Lower mantle and core dynamo evolution. *Journal of Geophysical Research: Planets*, 119, 1061–1077. https://doi.org/10.1002/2013JE004494
- Fleck, R. J., Sutter, J. F., & Elliot, D. H. (1977). Interpretation of discordant ⁴⁰Ar/³⁹Ar age-spectra of Mesozoic tholeiites from Antarctica. *Geochimica et Cosmochimica Acta*, 41, 15–32.
- Fuller, M. (1974). Lunar magnetism. Reviews of Geophysics and Space Physics, 12(1), 23-70. https://doi.org/10.1029/RG012i001p00023
- Fuller, M., Meshkov, E., Cisowski, S. M., & Hale, C. J. (1979). On the natural remanent magnetism of certain mare basalts (pp. 2211–2233). Proceedings of the Lunar and Planetary Science Conference, Houston, TX.
- Garrick-Bethell, I., & Weiss, B. P. (2010). Kamacite blocking temperatures and applications to lunar magnetism. Earth and Planetary Science Letters, 294(1–2), 1–7. https://doi.org/10.1016/j.epsl.2010.02.013
- Garrick-Bethell, I., Weiss, B. P., Shuster, D. L., & Buz, J. (2009). Early lunar magnetism. Science, 323, 356–359. https://doi.org/10.1126/science.1166804
- Garrick-Bethell, I., Weiss, B. P., Shuster, D. L., Tikoo, S. M., & Tremblay, M. M. (2017). Further evidence for early lunar magnetism from troctolite 76535. *Journal of Geophysical Research: Planets*, 121, 1–18. https://doi.org/10.1002/2016JE005154
- Gattacceca, J., Suavet, C., Rochette, P., Weiss, B. P., Winklhofer, M., Uehara, M., et al. (2014). Metal phases in ordinary chondrites: Magnetic hysteresis properties and implications for thermal history. *Meteoritics & Planetary Sciences*, 49(4), 652–676. https://doi.org/10.1111/maps.12268
- Haggerty, S. E., Boyd, F. R., Bell, P. M., Finger, L. W., & Bryan, W. B. (1970). Opaque minerals and olivine in lavas and breccias from Mare Tranquillitatis (Vol. 1, pp. 513–538). Proceedings of the Apollo 11 Lunar Science Conference, Houston, TX.
- Jourdan, F., & Renne, P. R. (2007). Age calibration of the Fish Canyon sanidine 40 Ar/39 Ar dating standard using primary K-Ar standards. Geochimica et Cosmochimica Acta, 71(2), 387–402.
- Kletetschka, G., & Wieczorek, M. A. (2017). Fundamental relations of mineral specific magnetic carriers for paleointensity determination. *Physics of the Earth and Planetary Interiors*, 272, 44–49. https://doi.org/10.1016/j.pepi.2017.09.008
- Konrad, W., & Spohn, T. (1997). Thermal history of the Moon: Implications for an early core dynamo and post-accretional magmatism. Advances in Space Research, 19(10), 1511–1521. https://doi.org/10.1016/S0273-1177(97)00364-5
- Kuiper, K. F., Deino, A., Hilgen, F. J., Krijgsman, W., Renne, P. R., & Wijbrans, J. R. (2008). Synchronizing Rock Clocks of Earth History. Science, 320(5875), 500–504.
- Laneuville, M., Wieczorek, M. A., Breuer, D., Aubert, J., Morard, G., & Rückriemen, T. (2014). A long-lived lunar dynamo powered by core crystallization. *Earth and Planetary Science Letters*, 401, 251–260. https://doi.org/10.1016/j.epsl.2014.05.057
- Lawrence, K., Johnson, C., Tauxe, L., & Gee, J. (2008). Lunar paleointensity measurements: Implications for lunar magnetic evolution. *Physics of the Earth and Planetary Interiors*, 168, 71–87. https://doi.org/10.1016/j.pepi.2008.05.007
- Le Bars, M., Wieczorek, M. A., Karatekin, O., Cébron, D., & Laneuville, M. (2011). An impact-driven dynamo for the early Moon. *Nature*, 479, 215–218. https://doi.org/10.1038/nature10565
- Lindquist, A. K., Feinberg, J. M., Harrison, R. J., Loudon, J. C., & Newell, A. J. (2015). Domain wall pinning and dislocations: Investigating magnetite deformed under conditions analogous to nature using transmission electron microscopy. *Journal of Geophysical Research:* Solid Earth, 120(3), 1415–1430. https://doi.org/10.1002/2014JB011335
- Lowrie, W., & Kent, D. V. (1978). Characteristics of VRM in Oceanic Basalts. Journal of Geophysics, 44(200), 297-315.
- Lyons, P. C., Krogh, T. E., Kwok, Y. Y., Davis, D. W., Outerbridge, W. F., & Evans, H. T., Jr. (2006). Radiometric ages of the Fire Clay tonstein [Pennsylvanian (Upper Carboniferous), Westphalian, Duckmantian]: A comparison of U-Pb zircon single-crystal ages and 40Ar/39Ar sanidine single-crystal plateau ages. *International Journal of Coal Geology*, 67(4), 259–266.
- Machlus, M. L., Shea, E. K., Hemming, S. R., Ramezani, J., & Rasbury, E. T. (2020). An assessment of sanidine from the Fire Clay tonstein as a Carboniferous ⁴⁰Ar/³⁹Ar monitor standard and for inter-method comparison to U-Pb zircon geochronology. *Chemical Geology*, 539.

STRAUSS ET AL. 19 of 21



- McDougall, I., & Harrison, T. M. (1977). Geochronology and thermochronology by the 40 Ar/39 Ar method. New York, NY: Oxford University Press
- Mercer, C. M., & Hodges, K. V. (2016). ArAR—A software tool to promote the robust comparison of K-Ar and ⁴⁰Ar/³⁹Ar dates published using different decay, isotopic, and monitor-age parameters. *Chemical Geology*, 440, 148–163.
- Meyer, C. (2011). The lunar sample compendium. Retrieved from https://www-curator.jsc.nasa.gov/lunar/lsc/index.cfm
- Mighani, S., Wang, H., Shuster, D. L., Borlina, C. S., Nichols, C. I. O., & Weiss, B. P. (2020). The end of the lunar dynamo. *Science Advances*, 6, eaax0883.
- NASA Manned Spacecraft Center. (1972). Apollo 16 preliminary science report (Tech. Rep. NASA SP-315).U.S.A.: National Aeronautics and Space Administration.
- Open University, T. (2018). The virtual microscope for earth sciences project: Apollo collections. Retrieved from https://www.virtualmicroscope.org/collections/apollo
- Pike, C. R., Roberts, A. P., & Verosub, K. L. (1999). Characterizing interactions in fine magnetic particle systems using first order reversal curves. *Journal of Applied Physics*, 85, 6660–6667.
- Renne, P. R., Balco, G., Ludwig, K. R., Mundil, R., & Min, K. (2011). Response to the comment by W.H. Schwarz et al. on "Joint determination of 40K decay constants and ⁴⁰Ar*/⁴⁰K for the Fish Canyon sanidine standard, and improved accuracy for ⁴⁰Ar/³⁹Ar geochronology" by P.R. Renne et al. *Geochimica et Cosmochimica Acta*, 75(17), 5097–5100.
- Renne, P. R., Deino, A. L., Hames, W. E., Heizler, M. T., Hemming, S. R., Hodges, K. V., et al. (2009). Data reporting norms for ⁴⁰Ar/³⁹Ar geochronology. *Quaternary Geochronology*, 4, 346–352. https://doi.org/10.1016/j.quageo.2009.06.005
- Rhodes, J. M., Blanchard, D. P., Dungan, M. A., Brannon, J. C., & Rodgers, K. V. (1977). Chemistry of Apollo 12 mare basalts: Magma types and fractionation processes (pp. 1305–1338). Proceedings of 8th Lunar Science Conference, Houston, TX. https://doi.org/10.1007/s13398-014-0173-7.2
- Roberts, A. P., Almeida, T. P., Church, N. S., Harrison, R. J., Heslop, D., Li, Y., et al. (2017). Resolving the Origin of Pseudo-Single Domain Magnetic Behavior. *Journal of Geophysical Research*: Solid Earth, 122(12), 9534–9558. https://doi.org/10.1002/2017JB014860
- Roberts, A. P., Pike, C. R., & Verosub, K. L. (2000). First-order reversal curve diagrams: A new tool for characterizing the magnetic properties of natural samples. *Journal of Geophysical Research*, 105(B12), 28461–28475. https://doi.org/10.1029/2000JB900326
- Roberts, A. P., Tauxe, L., Heslop, D., Zhao, X., & Jiang, Z. (2018). A Critical Appraisal of the "Day" Diagram. Journal of Geophysical Research: Solid Earth, 123, 2618–2644. https://doi.org/10.1002/2017JB015247
- Runcorn, S. K. (1996). The formation of the lunar core. Geochimica et Cosmochimica Acta, 60(7), 1205–1208. https://doi. org/10.1016/0016-7037(96)00024-5
- Scheinberg, A. L., Soderlund, K. M., & Elkins-Tanton, L. T. (2018). A basal magma ocean dynamo to explain the early lunar magnetic field. Earth and Planetary Science Letters, 492, 144–151.
- Scheinberg, A. L., Soderlund, K. M., & Schubert, G. (2015). Magnetic field generation in the lunar core: The role of inner core growth. *Icarus*, 254, 62–71. https://doi.org/10.1016/j.icarus.2015.03.013
- Setera, J. B., Turrin, B. D., Herzog, G. F., VanTongeren, J. A., Delaney, J. S., & Swisher, C. C., III (2020). ⁴⁰Ar/J³⁹Ar thermochronology for sub-milligram samples using a Ta-platform micro-furnace, with illustrations from the Bushveld Complex. *Geochemistry, Geophysics, Geosystems*, e2020GC009182. 1–9. https://doi.org/10.1029/2020GC009182
- Shea, E. K., Weiss, B. P., Cassata, W. S., Shuster, D. L., Tikoo, S. M., Gattacceca, J., et al. (2012). A long-lived lunar core dynamo. *Science*, 335, 453–456. https://doi.org/10.1126/science.1215359
- Shuster, D. L., & Cassata, W. S. (2015). Paleotemperatures at the lunar surfaces from open system behavior of cosmogenic 38-Ar and radiogenic 40-Ar. *Geochimica et Cosmochimica Acta*, 155, 154–171. https://doi.org/10.1016/j.gca.2015.01.037
- Stanley, S., Tian, B. Y., Weiss, B. P., & Tikoo, S. M. (2017). The ancient lunar dynamo: How to resolve the intensity and duration conundrums. *Lunar and planetary science*, 48, 1462. https://doi.org/10.1002/2016JE005154
- Stegman, D. R., Jellinek, A. M., Zatman, S. A., Baumgardner, J. R., & Richards, M. A. (2003). An early lunar core dynamo driven by thermochemical mantle convection. *Nature*, 421, 143–146. https://doi.org/10.1038/nature01267
- Steiger, R. H., & Jäger, E. (1977). Subcommission on geochronology: Convention on the use of decay constants in geo- and cosmochemistry. Earth and Planetary Science Letters, 36(3), 359–362.
- $Stephenson, A.~(1993). \ Three-axis static alternating field demagnetization of rocks and the identification of natural remanent magnetization, gyroremanent magnetization, and anisotropy. \textit{Journal of Geophysical Research}, 98(B1), 373–381. \\ \underline{https://doi.org/10.1029/92JB01849}$
- Stephenson, A., & Collinson, D. W. (1974). Lunar magnetic field palaeointensities determined by an anhysteretic remanent magnetization method. Earth and Planetary Science Letters, 23, 220–228. https://doi.org/10.1016/0012-821X(74)90196-4
- Stettler, A., Eberhardt, P., Geiss, J., Grögler, N., & Maurer, P. (1973). Ar39-Ar40 ages and Ar37-Ar38 exposure ages of lunar rocks (Vol. 4, pp. 1865–1888). Proceedings of Lunar and Planetary Science, Houston, TX.
- Stöffler, D., Ryder, G., Ivanov, B. A., Artemieva, N. A., Cintala, M. J., & Grieve, R. A. F. (2006). Cratering history and lunar chronology. Reviews in Mineralogy and Geochemistry, 60, 519–596. https://doi.org/10.2138/rmg.2006.60.05

 Strangway, D. W., Gose, W. A., Pearce, G. W., & Carnes, J. G. (1973). Magnetism and the history of the Moon (Vol. 10, pp. 1178). AIP Con-
- ference Proceedings. https://doi.org/10.1063/1.2946764

 Strauss B. (2020) Symplemental Data for "Constraining the decline of the lungr dynamo field at ~ 3.1 Ca through paleomegapatic analysis of
- Strauss, B. (2020). Supplemental Data for "Constraining the decline of the lunar dynamo field at ≈ 3.1 Ga through paleomagnetic analysis of Apollo 12 mare basalts". https://doi.org/10.18434/mds2-2303
- Stys, C., & Dumberry, M. (2020). A past lunar dynamo thermally driven by the precession of its inner core. *Journal of Geophysical Research:* Planets, 125 https://doi.org/10.1029/2020JE006396
- Suavet, C., Weiss, B. P., Cassata, W. S., Shuster, D. L., Gattacceca, J., Chan, L., et al. (2013). Persistence and origin of the lunar core dynamo. *Proceedings of the National Academy of Sciences of the United States of America*, 110(21), 8453–8458. https://doi.org/10.1073/pnas.1300341110
 Suavet, C., Weiss, B. P., & Grove, T. L. (2014). Controlled-atmosphere thermal demagnetization and paleointensity analyses of extraterres-
- trial rocks. Geochemistry, Geophysics, Geosystems, 15, 2733–2742. https://doi.org/10.1002/2013GC005215 Swartzendruber, L. J., Itkin, V. P., & Alcock, C. B. (1991). The Fe-Ni (iron-nickel) system. Journal of Phase Equilibria, 12(3), 288–312.
- Tauxe, L., & Staudigel, H. (2004). Strength of the geomagnetic field in the Cretaceous Normal Superchron: New data from submarine basaltic glass of the Troodos Ophiolite. *Geochemistry, Geophysics, Geosystems*, 5(2). https://doi.org/10.1029/2003GC000635
- Taylor, J. (1997). Introduction to error analysis, the study of uncertainties in physical measurements: Herndon, VA: University Science Books. Tikoo, S. M., Weiss, B. P., Buz, J., Lima, E. A., Shea, E. K., Melo, G., et al. (2012). Magnetic fidelity of lunar samples and implications for an ancient core dynamo. Earth and Planetary Science Letters, 337–338, 93–103. https://doi.org/10.1016/j.epsl.2012.05.024
- Tikoo, S. M., Weiss, B. P., Cassata, W. S., Shuster, D. L., Gattacceca, J., Lima, E. A., et al. (2014). Decline of the lunar core dynamo. *Earth and Planetary Science Letters*, 404, 89–97. https://doi.org/10.1016/j.epsl.2014.07.010

STRAUSS ET AL. 20 of 21



- Tikoo, S. M., Weiss, B. P., Shuster, D. L., Suavet, C., Wang, H., & Grove, T. L. (2017). A two-billion-year history for the lunar dynamo. *Science Advances*, 3, 1–10. https://doi.org/10.1126/sciadv.1700207
- $Turner, G. (1971). Argon 40-Argon 39 dating: The optimization of irradiation parameters. \textit{Earth and Planetary Science Letters}, 10, 227-234. \\ https://doi.org/10.1016/0012-821X(71)90010-0$
- Turrin, B. D., Gutmann, J. T., & Swisher, C. C., III (2008). A 13 ± 3 ka age determination of a tholeitte, Pinacate volcanic field, Mexico, and improved methods for ⁴⁰Ar/³⁹Ar dating of young basaltic rocks. *Journal of Volcanology and Geothermal Research*, 177, 850–859.
- Turrin, B. D., Swisher, C. C., III, & Deino, A. L. (2010). Mass discrimination monitoring and intercalibration of dual collectors in noble gas mass spectrometer systems. *Geochemistry, Geophysics, Geosystems*, 11(8), 1–20. https://doi.org/10.1029/2009GC003013
- Udry, A., Wilbur, Z. E., Rahib, R. R., McCubbin, F. M., Vander Kaaden, K. E., McCoy, T. J., et al. (2019). Reclassification of four aubrites as enstatite chondrite impact melts: Potential geochemical analogs for Mercury. *Meteoritics & Planetary Sciences*, 1–26. https://doi.org/10.1111/maps.13252
- Uehara, M., Gattacceca, J., Leroux, H., Jacob, D., & van der Beek, C. J. (2011). Magnetic microstructures of metal grains in equilibrated ordinary chondrites and implications for paleomagnetism of meteorites. *Earth and Planetary Science Letters*, 306(3–4), 241–252. https://doi.org/10.1016/j.epsl.2011.04.008
- Walker, D., Kirkpatrick, R. J., Longhi, J., & Hays, J. F. (1976). Crystallization history of lunar picritic basalt sample 12002: Phase-equilibria and cooling-rate studies. *Bulletin of the Geological Society of America*, 87(5), 646–656. https://doi.org/10.1130/0016-7606(1976)87\646: CHOLPB\2.0.CO:2
- Warner, J. (1970). NASA technical report R-353: Apollo 12 lunar sample information (Tech. Rep. NASA TR R-353). Washington, DC: NASA. Wasilewski, P. J. (1974). Magnetic remanence mechanisms in iron and iron-nickel alloys, metallographic recognition criteria and implications for lunar sample research. The Moon, 9, 335–354.
- Watson, G. S. (1956). Analysis of dispersion on a sphere. *Geophysical Supplements to The Monthly Notices of The Royal Astronomical Society*, 7, 160–161.
- Weiss, B. P., & Tikoo, S. M. (2014). The lunar dynamo. Science, 346(6214), 10. https://doi.org/10.1126/science.1246753
- Zhang, N., Parmentier, E. M., & Liang, Y. (2013). A 3-D numerical study of the thermal evolution of the Moon after cumulate mantle overturn: The importance of rheology and core solidification. *Journal of Geophysical Research: Planets, 118*, 1789–1804. https://doi.org/10.1002/jgre.20121

STRAUSS ET AL. 21 of 21